

Triple-ionised carbon associated with the low-density neutral hydrogen gas at $1.7 < z < 3.3$: the integrated $N_{\text{HI}}-N_{\text{CIV}}$ relation[★]

T.-S. Kim^{1,2,3†}, R. F. Carswell⁴, C. Mongardi⁵, A. M. Partl², J. P. Mückel², P. Barai¹, S. Cristiani¹

¹ *INAF, Osservatorio Astronomico di Trieste, Via G. B. Tiepolo, 11, 34143, Trieste, Italy*

² *Leibniz-Institut für Astrophysik Potsdam, An der Sternwarte 16, D-14482 Potsdam, Germany*

³ *Department of Astronomy, University of Wisconsin, 475 North Charter Street, Madison, WI 53706, USA*

⁴ *Institute of Astronomy, Madingley Road, Cambridge CB3 0HA*

⁵ *Dipartimento di Fisica, Sezione di Astronomia, Università di Trieste, Via G. B. Tiepolo 11, I-34143 Trieste, Italy*

Accepted Recieved

ABSTRACT

From the Voigt profile fitting analysis of 183 intervening C IV systems at $1.7 < z < 3.3$ in 23 high-quality UVES/VLT and HIRES/Keck QSO spectra, we find that a majority of C IV systems ($\sim 75\%$) display a well-characterised scaling relation between integrated column densities of H I and C IV with a negligible redshift evolution, when column densities of all the H I and C IV components are integrated within a given $\pm 150 \text{ km s}^{-1}$ range centred at the C IV flux minimum. The integrated C IV column density $N_{\text{CIV,sys}}$ increases with $N_{\text{HI,sys}}$ at $\log N_{\text{HI,sys}} \in [14, 16]$ and $\log N_{\text{CIV,sys}} \in [11.8, 14.0]$, then becomes almost independent of $N_{\text{HI,sys}}$ at $\log N_{\text{HI,sys}} \geq 16$, with a large scatter: at $\log N_{\text{HI,sys}} \in [14, 22]$, $\log N_{\text{CIV,sys}} = \left[\frac{C_1}{\log N_{\text{HI,sys}} + C_2} \right] + C_3$, with $C_1 = -1.90 \pm 0.55$, $C_2 = -14.11 \pm 0.19$ and $C_3 = 14.76 \pm 0.17$, respectively. The steep (flat) part is dominated by Si IV-free (Si IV-enriched) C IV systems. Extrapolating the $N_{\text{HI,sys}}-N_{\text{CIV,sys}}$ relation implies that most absorbers with $\log N_{\text{HI}} \leq 14$ are virtually C IV-free. The $N_{\text{HI,sys}}-N_{\text{CIV,sys}}$ relation does not hold for individual components, clumps or the integrated velocity range less than $\pm 100 \text{ km s}^{-1}$. This is expected if the line-of-sight extent of C IV is smaller than H I and $N_{\text{CIV,sys}}$ decreases more rapidly than $N_{\text{HI,sys}}$ at the larger impact parameter, regardless of the location of the H I+C IV gas in IGM filaments or in intervening galactic halos.

Key words: cosmology: observation – intergalactic medium – quasars: absorption lines

1 INTRODUCTION

The numerous, narrow absorption lines observed blueward of the Ly α emission line in spectra of background QSOs are mostly produced by the warm ($\sim 10^4 \text{ K}$), photoionised, intergalactic neutral hydrogen (H I) gas. These absorption lines or *absorbers* are known as the Ly α forest or the intergalactic medium (IGM) and have a H I column den-

sity (N_{HI}) less than 10^{17} cm^{-2} . Being a dominant reservoir of the baryons at all cosmic epochs and tracing the underlying dark matter in a simple manner, the Ly α forest has been used as a cosmological tool to study the primordial power spectrum and the formation and evolution of the large-scale matter distribution (Cen et al. 1994; Davé et al. 1999; Kim et al. 2004; McDonald et al. 2006; Palanque-Delabrouille et al. 2013).

Absorption lines redward of the Ly α emission are produced by metal species which also contribute a small fraction of the lines in the Ly α forest. The most common metal transition found in QSO spectra is the triply ionised carbon doublet, C IV $\lambda\lambda$ 1548.204, 1550.778. Roughly half of the Ly α forest with $N_{\text{HI}} \geq 10^{14.5} \text{ cm}^{-2}$ is C IV-enriched at $z \sim 3$ (Cowie et al. 1995; Tytler et al. 1995; Songaila 1998).

[★] Based on data obtained with UVES (Ultraviolet and Visual Echelle Spectrograph) at the VLT (Very Large Telescope), Paranal, Chile, from the ESO archive and obtained with HIRES (High Resolution Spectrometer) at Keck, Hawaii, USA, from the Keck archive.

[†] E-mail: kim@oats.inaf.it

The C IV enrichment has even been suggested at lower $N_{\text{H I}}$ (Songaila 1998; Ellison et al. 2000; Schaye et al. 2003). The triply ionised silicon doublet, Si IV $\lambda\lambda$ 1393.760, 1402.772, is also common, but is usually associated with a higher $N_{\text{H I}}$. An observational rule of thumb is that higher- $N_{\text{H I}}$ absorbers are associated with more metal species and stronger, multi-component metal lines. Low-ionisation metal transitions, such as Mg II and C II, are mostly found at $N_{\text{H I}} \geq 10^{16} \text{ cm}^{-2}$. Absorbers with $N_{\text{H I}} \geq 10^{17.2} \text{ cm}^{-2}$ (Lyman limit systems or LLSs) display a wide range of metal species and ionisations (Steidel 1990; Levshakov et al. 2003; Prochaska et al. 2006; Lehner et al. 2013) and are thought to be associated with outflows/infall in outer halos (Jenkins et al. 2005; Faucher-Giguère & Kereš 2011; Kacprzak et al. 2011; Ribaldo et al. 2011; Bouché et al. 2012; Lehner et al. 2013), or with extended disks/inner halos at ≤ 10 –20 kpc, e.g. an analogue of intermediate/high velocity clouds of the Milky Way or merger remnants (Thilker et al. 2004; Lehner et al. 2009; Stocke et al. 2010).

Heavy elements are produced in stars which occur in galaxies. However, the Ly α forest does not have an *in situ* star formation due to its high temperature and low gas density at $\sim 10^{-4} \text{ cm}^{-3}$, so any metals associated with the Ly α forest must have been transferred there from galaxies in some way. Therefore, since the discovery of metals associated with the Ly α forest, studies on the IGM enrichment have been focused mainly on two topics: *what* is the enrichment mechanism and *where* is the metal-enriched gas located.

Among several proposed scenarios, such as the enrichment by Population III stars at $10 < z < 20$ (Ostriker & Gnedin 1996; Haiman & Loeb 1997) and by dynamical removal of metals from galaxies through a merger or tidal interaction (Gnedin & Ostriker 1997; Gnedin 1998; Aguirre et al. 2001b), the scenario with most support from observations is galactic-scale outflows or galactic winds (Davé et al. 1998; Aguirre et al. 2001a; Schaye et al. 2003; Springel & Hernquist 2003; Murray et al. 2005; Oppenheimer & Davé 2006).

Although detailed outflow mechanisms are still far from being clear, in the simplified, qualitative picture, galactic outflows driven by supernovae or by young OB stars disperse metal-enriched gas from disks to halos, from halos to the surrounding IGM. The extent of galactic winds are limited by the radiative and mechanical energy loss and the pressure of the infalling, surrounding medium. One of the predictions by the outflow models is the volume-averaged overdensity–metallicity relation, clearly shown in their Fig. 1 by Aguirre et al. (2001b) (but see also Springel & Hernquist (2003) and Oppenheimer & Davé (2006)). The IGM metallicity drops off sharply at overdensities smaller than a drop-off overdensity. Above this drop-off overdensity, however, the IGM metallicity is independent of overdensities. The exact shape of this overdensity–metallicity relation depends on the outflow velocity, its onset time and the interaction with the surrounding IGM. With a higher outflow velocity, a longer traveling time, a low pressure of the local IGM and a small potential well of outflow galaxies, outflows can enrich a lower-density IGM. With a smaller outflow velocity and a strong galactic potential well, metals are likely to be located mostly inside a virial radius of parents galaxies, never escap-

ing in to the IGM, thus leaving the typical IGM virtually metal-free

Galactic-scale outflows are a well-established phenomenon both at lower and higher redshifts. In local starburst galaxies, galactic outflows operate on scales of 10–100 kpc, sometimes even at $\sim 1000 \text{ km s}^{-1}$ scale, enough to escape the parents galaxies (Strickland et al. 2004; Martin 2005, 2006; Tremonti et al. 2007). The COS-Halos survey at $z \sim 0.2$ also shows that star-forming galaxies of $\sim 1 L_*$ commonly have a large-scale O VI outflow up to 150 kpc (Tumlinson et al. 2011; Werk et al. 2013, 2014). At $z \sim 3$, Lyman break galaxies often show outflows with velocities of several hundred km s^{-1} (Pettini et al. 2002; Shapley et al. 2003; Erb et al. 2012). High ions, such as O VI and C IV, in sub-damped Ly α systems (sub-DLAs, $N_{\text{H I}} \sim 10^{19-20.3} \text{ cm}^{-2}$) and damped Ly α systems (DLAs, $N_{\text{H I}} \geq 10^{20.3} \text{ cm}^{-2}$) also reinforce the notion that the presence of inflows and outflows is common at $z \sim 3$ (Fox et al. 2007a,b; Lehner et al. 2014). In addition, Steidel et al. (2010) used the close galaxy-galaxy pairs at $z \sim 2.2$ to study the gas surrounding foreground galaxies in the spectra of background galaxies at the impact parameters at 3–125 physical kpc. They found that foreground galaxies are surrounded by metal-enriched gaseous envelopes and that the strength of metal ions, such as C IV and C II, decreases as a power law up to a certain impact parameter, then decreases rapidly beyond it. This point occurs at $\sim 250 \text{ kpc}$ for H I Ly α at $N_{\text{H I}} \sim 10^{13.25} \text{ cm}^{-2}$ and at $\sim 80 \text{ kpc}$ for C IV at $N_{\text{C IV}} \sim 10^{13.5} \text{ cm}^{-2}$.

We present new results on the well-characterised $N_{\text{H I}} - N_{\text{C IV}}$ relation of H I absorbers at $N_{\text{H I}} \sim 10^{12.5-22} \text{ cm}^{-2}$ at $1.7 < z < 3.3$, using 23 high-resolution ($\sim 6.7 \text{ km s}^{-1}$), high-signal-to-noise ($S/N \sim 50$ per pixel for H I and $S/N \sim 100$ for C IV) spectra obtained with UVES at the VLT and HIRES at Keck. The observed $N_{\text{H I}} - N_{\text{C IV}}$ relation is an equivalent to the theoretical overdensity–metallicity relation, as the overdensity is related to $N_{\text{H I}}$ and the metallicity can be estimated from measured ion column densities, assuming photoionisation equilibrium and the ambient UV background (Cowie et al. 1995; Hui & Gnedin 1997; Rauch et al. 1997; Davé et al. 1999; Schaye 2001). Although our study does not have a deep redshift survey to look for galaxies associated with C IV gas, our C IV detection limit for a typical line of sight is $N_{\text{C IV}} \sim 10^{12} \text{ cm}^{-2}$. This limit is much lower than $N_{\text{C IV}} \sim 10^{13.5} \text{ cm}^{-2}$ of the study by Steidel et al. (2010). Our data explore a lower- $N_{\text{C IV}}$ gas, i.e. far away from nearby galaxies and provide new observational constraints on the outflow mechanisms and the metal abundance at low-density H I absorbers.

To obtain a robust $N_{\text{H I}}$ for C IV-enriched H I absorbers, we performed the Voigt profile fitting analysis including all the available high-order Lyman series, cf. Kim et al. (2013). To derive the physical conditions of C IV-producing gas, we performed the photoionisation modelling using the code CLOUDY version 13.03 (Ferland et al. 2013).

Figure 1 illustrates a snapshot from a typical cosmological hydrodynamic simulation taken from Barai et al. (2015) at $z = 2$. The left and right panels display the distribution of H I and C IV, their column density range indicated as a color bar on top. The two arrows in each panel sample a typical line of sight in observations, which passes through massive galaxies, dwarf galaxies, IGM filaments close and

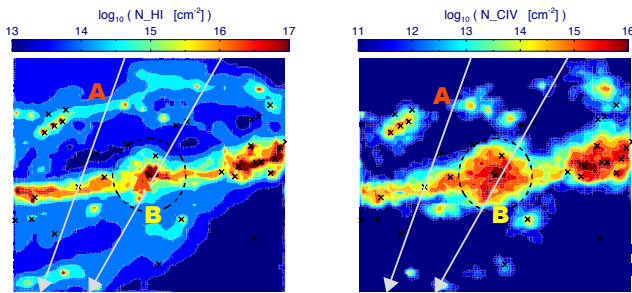


Figure 1. The simulated distribution of H I (the left panel) and C IV (the right panel) at $z = 2$, centred around a galaxy with a halo mass of $10^{11} M_{\odot}$ in the box size of 1 comoving Mpc. The snapshots are taken from the run M25std of Barai et al. (2015). The black dashed circle denotes the galaxy virial radius of 150 kpc. The black crosses mark the centre of other galaxies or stellar subhalos identified within this volume. The two arrows represent a typical line of sight in observations, which passes through the central galaxy as well as halos of other galaxies, metal-enriched filaments and metal-free filaments. The gases at the positions marked as “A” and “B” have a similar $N_{\text{H I}}$ and $N_{\text{C IV}}$, but are located in a different place. A coloured, online version provides a better view.

far from galaxies and voids. A gas having a similar $N_{\text{H I}}$ and $N_{\text{C IV}}$ can be located in a different environment.

In practice, the observed lines of sight provide an ensemble of the gas at a variety of $N_{\text{H I}}$ and $N_{\text{C IV}}$ as well as many different locations, i.e. filaments vs halos within a virial radius. Therefore, a scatter $N_{\text{H I}}-N_{\text{C IV}}$ relation might be expected, as seen by Simcoe et al. (2004). Indeed, our H I+C IV components aligned within 5 km s^{-1} from each other display a scatter plot on the $N_{\text{H I}}-N_{\text{C IV}}$ plane, but the scatter can be used to constrain the physical condition of absorbing gas. We also find that a well-characterised, integrated $N_{\text{H I}}-N_{\text{C IV}}$ relation exists for the low-density Si IV-free C IV systems defined as H I and C IV profiles within a fixed velocity ranged centred at the C IV flux minimum.

This paper is organised as follows. Section 2 describes the analysed data. In Section 3, we present the Voigt profile fitting analysis in detail. Section 4 introduces a new working definition on a system and a clump to describe our H I+C IV sample. As Sections 3 and 4 are rather technical, casual readers might skip directly to Section 5 in which our main results on the integrated $N_{\text{H I}}$ and $N_{\text{C IV}}$ relation of C IV systems and clumps are presented. Results on the aligned components are presented in Section 6. Implications of our results are explored in Section 7. Section 8 presents the summary.

The logarithmic column density of an ion M , $\log N_M$, is expressed as $\log(N_M/\text{cm}^{-2})$. Throughout the paper, the cosmological parameters are assumed to be the matter density $\Omega_m = 0.24$, the cosmological constant $\Omega_{\Lambda} = 0.73$ and the present-day Hubble constant $H_0 = 100 h \text{ km s}^{-1} \text{ Mpc}^{-1}$ with $h = 0.7$ in accord with WMAP measurements (Jarosik et al. 2011). We also ask readers to look at the online, coloured versions of any figures to resolve any ambiguities.

2 DATA

Table 1 lists the 23 QSOs and their spectra analysed in this study. The 21 raw spectra of the 23 QSOs were taken from the ESO VLT/UVES archive, while the remaining 2 QSOs were taken from the Keck/HIRES archive. As this sample was designed to study the low-density IGM at $2 < z < 3.5$, the first selection criterion was QSOs without any strong DLAs and only few LLSs in any one sightline. In addition, in order to cover high-order Lyman lines to obtain a reliable column density of saturated H I, the second selection criterion was only QSOs with high S/N and a long, continuous wavelength coverage. 18 of the 21 UVES spectra were analysed in Kim et al. (2007, 2013) and the other three were described by Kim et al. (2004). Most UVES spectra cover from 3050 \AA (a natural cutoff due to the Earth’s atmosphere) to 10000 \AA (due to the limitation of the optical instrument), with some gaps due to the CCD detector configuration. The 2 HIRES spectra are described by Boksteinberg & Sargent (2015). A *HST*/STIS echelle spectrum is available for J2233–606¹ (Savaglio et al. 1999), so it was used here to extend its wavelength coverage down to 2300 \AA .

The wavelengths for all spectra are heliocentric corrected, and the spectral resolution is $R \sim 45\,000$ (or $\sim 6.7 \text{ km s}^{-1}$). The UVES/STIS spectra and the HIRES spectra are sampled at 0.05 \AA and 0.04 \AA , respectively.

To avoid the proximity effect, the region of $5,000 \text{ km s}^{-1}$ blueward of the QSO’s Ly α emission was excluded from the Ly α H I study. Note that this velocity cut also eliminates any absorption lines due to the ejecta of mini-BAL (Broad Absorption Line) QSOs in the sample. This sets the highest redshift searched for C IV in each QSO. The lowest search redshift of C IV doublets is set by the QSO’s Ly α emission line itself. Below the Ly α emission, C IV becomes blended with the Ly α forest and its detection is likely to be incomplete regardless of its detection limit. In addition, obtaining a reliable $N_{\text{H I}}$ of saturated H I lines requires high-order Lyman lines, which further limits the useful redshift range. The signal-to-noise (S/N) ratio also affects a profile fitting process, with a higher S/N providing a more reliable deblending of saturated lines. These requirements set the analysed redshift range for H I and C IV of each spectra, which is listed in the third column in Table 1. Section 3 discusses the coverage of high-order lines and the S/N for obtaining a robust column density in more detail.

In addition to the CCD detector gaps, the UVES spectra are contaminated by numerous telluric lines above 6200 \AA , particularly at $6276\sim 6319 \text{ \AA}$ ($3.055 < z_{\text{C IV}} < 3.080$) in the redshift range of interest. These regions are also excluded. Where there are such gaps in the coverage, multiple search ranges are listed in the third column in Table 1. We did not exclude any other regions, such as the ones around a DLA or a sub-DLA, and included all the detected high- $N_{\text{H I}}$ absorbers in our analysis.

The fourth column of Table 1 lists the S/N per pixel in the central parts of the H I and C IV regions. Since the S/N varies from spectrum to spectrum and even along the same spectrum, the listed S/N is only a rough indicator of the data quality. The typical S/N is $30\sim 50$ in the Ly α forest region, while it is $10\sim 15$ in the Ly β forest region and even

¹ <http://www.stsci.edu/ftp/observing/hdf/hdfsouth/hdfs.html>

Table 1. Analysed QSOs

QSO	z_{em}^{a}	$z_{\text{H I, C IV}}$	S/N ^b	Inst.	ref. ^c	Notes
Q0055–269	3.656	2.663–3.054, 3.077–3.390	[29, 62]	UVES	1, 2, 3	
PKS2126–158	3.280	2.413–2.608, 2.669–3.055, 3.075–3.208	[100, 125]	UVES	1, 2, 3	
HS1425+6039	3.180	2.667–3.110	[83, 71]	HIRES	4	DLA at $z = 2.827$, sub-DLA at $z = 2.770$
Q0636+6801	3.175	2.863–3.105	[50, 67]	HIRES	4	
Q0420–388	3.115	2.670–2.615, 2.670–3.045	[125, 111]	UVES	1, 2, 3	sub-DLA at $z = 3.087$
HE0940–1050	3.082	2.498–2.716, 2.776–3.014	[83, 111]	UVES	1, 2, 3	
HE2347–4342	2.873	2.080–2.710, 2.770–2.809	[100, 100]	UVES	1, 2, 3	
HE0151–4326	2.781 ^d	2.072–2.710	[100, 125]	UVES	1	mini-BAL
Q0002–422	2.768	2.016–2.705	[87, 137]	UVES	1, 2, 3	
PKS0329–255	2.704	2.091–2.643	[38, 63]	UVES	1, 2, 3	
Q0453–423	2.657	1.978–2.595	[67, 100]	UVES	1, 2, 3	sub-DLA at $z = 2.305$
HE1347–2457	2.612 ^d	1.987–2.552	[63, 67]	UVES	1, 2, 3	
Q0329–385	2.435	2.001–2.378	[45, 83/45]	UVES	1, 2, 3	
HE2217–2818	2.413	1.979–2.355	[67, 100]	UVES	1, 2, 3	mini-BAL
Q0109–3518	2.405	1.976–2.348	[67, 91/140]	UVES	1, 2, 3	
HE1122–1648	2.404	1.975–2.346	[111, 200/71]	UVES	1, 2, 3	
HE0001–2340	2.264	1.993–2.211	[67, 80]	UVES	1	sub-DLA at $z = 2.187$
J2233–606 ^e	2.251	1.588–2.197	[33, 45]	UVES	1, 2, 3, 5	mini-BAL
PKS0237–23	2.222	1.975–2.167	[99, 136]	UVES	1, 2, 3	sub-DLA at $z = 1.673$
PKS1448–232	2.219	1.986–2.168	[57, 122/70]	UVES	1, 2, 3	
Q0122–380	2.191 ^d	1.977–2.140	[48, 77]	UVES	1, 2, 3	
Q1101–264	2.141	1.800–2.090 ^f	[67, 77]	UVES	1, 2, 3	sub-DLA at $z = 1.839$
HE1341–1020	2.138 ^d	1.972–2.086	[50, 63]	UVES	1	mini-BAL

^a The redshift is measured from the observed Ly α emission line of the QSOs.

^b The first and the second numbers separated by a comma in the brackets are the S/N per pixel estimated from the central parts of the H I and C IV regions, respectively. Due to an instrument setup which determines the wavelength ranges to be overlapped, some QSOs have a much higher S/N for part of the C IV region. In this case, two numbers are listed separated by “/”.

^c 1: Kim et al. (2004); 2: Kim et al. (2007); 3: Kim et al. (2013); 4: Boksenberg & Sargent (2015); 5: Savaglio et al. (1999)

^d The redshift estimated from the Ly α emission profile is uncertain as there are many absorption lines in the peak of the Ly α emission line or as the emission profile is non-Gaussian.

^e The *HST*/STIS E230M spectrum (Savaglio et al. 1999) is included in the analysis 3 since its observed wavelength at 2550–3057 Å covers high-order Lyman lines of saturated H I lines in the analysed redshift range.

^f Although H I Lyman lines higher than Ly β are not covered at $z < 1.972$, a robust H I column density of a sub-DLA at $z = 1.839$ can be obtained due to the damping wing. In order to increase the high- $N_{\text{H I}}$ absorbers in our sample, the redshift range for this QSO was extended to $z = 1.800$.

lower in the higher-order forest regions. On the other hand, the S/N ratio in the C IV region is in general higher. The S/N of the J2233–606 STIS spectrum is ~ 7 at ~ 2750 Å. As the S/N varies along the spectrum, the detection limit of H I Ly α and C IV also varies locally.

The 5th and 6th columns note the spectrograph used to obtain the spectrum and the references in which the same spectrum was analysed for other scientific objectives. Any strong intervening absorbers and/or mini-BAL QSOs are noted in the 7th column.

3 VOIGT PROFILE FITTING ANALYSIS

3.1 Brief description of the Voigt profile fitting procedure

We have fitted Voigt profiles to the absorption lines to obtain the absorption line parameters: the redshift z , the column density N in cm^{-2} and the Doppler parameter b ($= \sqrt{2}\sigma$, where σ is the standard deviation for a Gaussian distribution) in km s^{-1} .

Voigt profiles were fitted to the absorption lines using VPFIT (Carswell & Webb 2014), using the rest-frame wavelengths and the oscillator strengths provided with the program. The three versions of VPFIT were used to produce the final line parameters, versions 8.2, 9.5 and 10.2, depending on when the fitting analysis was performed. For the application here, the final results are very similar whichever version is used. Note that the line lists used in this work are similar

to, but not necessarily exactly the same as, those used previously (Kim et al. 2007, 2013), since small changes in the estimates for the local continuum or the removal/addition of weak column density components affect the detailed results.

Details of the methods used and caveats can be found in the documentation accompanying the program, and also in Carswell, Schaye & Kim (2002) and Kim et al. (2007). Here, we give a short description of the fitting procedure, following Kim et al. (2013).

First, each spectrum was divided into several chunks and normalised locally by connecting seemingly unabsorbed regions using the CONTINUUM/ECHELLE command in IRAF. Second, possible metal lines were searched for from the longest wavelength toward the shorter wavelength. All the identified metal lines were fitted first. Then, using them as presets, the rest of the absorption features were fitted as H I. When metal lines were blended with H I lines and/or other metal lines, all the blended lines were included in the fit simultaneously. To obtain reliable line parameters of saturated H I lines, all the available higher-order Lyman series such as Ly β and Ly γ were also included in the fit. Since there is no unique solution to the profile fitting, we imposed only one condition: a minimum number of necessary components to reach a reduced χ^2 value to be ≤ 1.2 , cf. Boksenberg & Sargent (2014). Note that the STIS E230M line spread function was used to fit the J2233–606 STIS spectrum.

The redshifts and b parameters for H I and C IV were allowed to vary *freely* to obtain a minimum χ^2 in VPFIT. The C IV absorbers found in QSO spectra are usually associated

with a saturated Ly α H I and have a multi-component unsaturated C IV. Even the higher order Lyman line profiles do not reveal velocity structures as detailed as those of C IV, at least in part because the thermal line broadening is greater for hydrogen than carbon due to the atomic mass difference. Consequently it is not generally possible to use H I to determine the C IV redshift. Indeed there is no physical reason to expect the velocity structure of C IV to closely follow that of H I, given that the peculiar velocity and bulk motions play a role in the kinematics of the absorbers. Moreover, studies of close QSO pairs show that H I and C IV display a different small-scale structure (Rauch et al. 2001). It has also been found that there is a velocity difference at 5–18 km s⁻¹ between the centroids of H I and C IV (Ellison et al. 2000).

During the simultaneous fit of different transitions of the same ions, we have often adjusted a small amount of the continuum placement to achieve a overall better fit result. Initially, the VPFIT continuum adjustment option was turned on. Then, comparing the unnormalised spectrum with the adjusted continuum, we decided whether to take the VPFIT adjustment as it was or to apply a slightly different continuum. With this re-adjusted new continuum, the entire spectrum was fitted again. We iterated the continuum re-adjustment and fitting several times until the satisfactory fits were obtained, finding some more previously unidentified metal lines and fixing any wrong line parameters previously obtained. The final iteration was done without the VPFIT continuum adjustment option.

Note that all the quoted errors of the fitted line parameters are directly from VPFIT. These do not include continuum uncertainties usually adopted in the Milky Way ISM studies, i.e. changing the continuum by ± 0.5 times the standard deviation of a local continuum (Sembach et al. 1991). We also note that VPFIT does not work like the apparent optical depth analysis (Savage & Sembach 1991), in that VPFIT looks for the best-fit solution by minimising χ^2 . This is not necessarily a lower limit column density for saturated lines. If the VPFIT column density errors are greater than 0.2–0.3 dex, the error estimates can be far from true for single saturated lines and one should treat the errors with caution (see the documents provided with VPFIT for more details, in particular Chapter 17). While the decomposition of absorption features depends on the local S/N and resolution, especially b parameters, the total column density integrated over a given velocity range is in general more securely determined.

3.2 A robust H I column density measurement

In general, C IV associated with the Ly α forest is *not* saturated, which provides a well-measured $N_{\text{C IV}}$ as long as blends by other lines are accounted for. On the other hand, H I Ly α associated with C IV is usually saturated. Therefore, without other information it is not possible to determine the H I component structure or, unless there are measurable damping wings, to obtain a reliable H I column density. For this reason we have chosen analyzed redshift ranges which ensure that at least Ly β is always available. Where possible, other Lyman lines with lower oscillator strength are also included in the Voigt profile fit to determine the reliable H I parameters. The atmospheric cutoff at 3050 Å sets a natural lowest redshift limit to cover the corresponding Ly β to

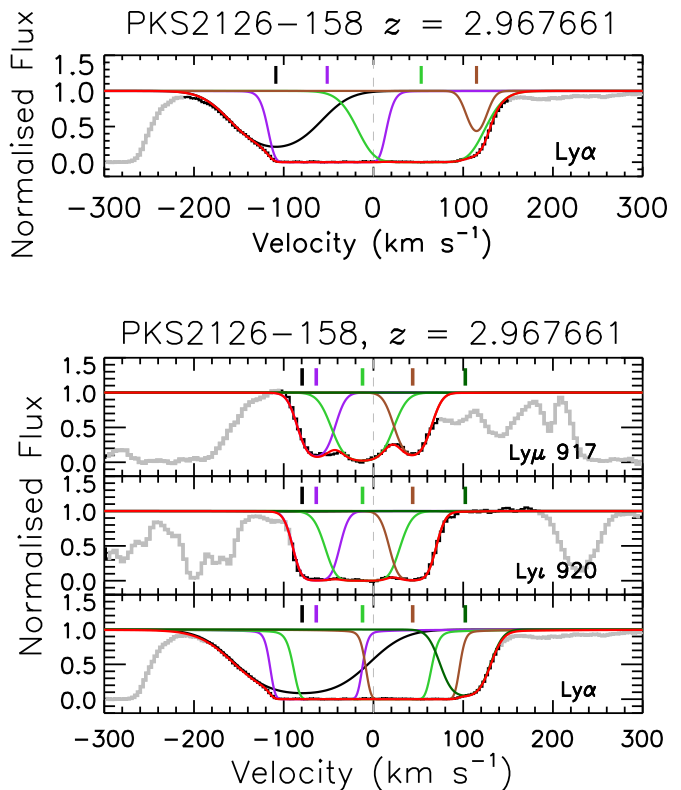


Figure 2. The normalised H I flux (black histogram) vs the relative velocity v of a C IV absorber at $z = 2.967661$ toward PKS2126–158. The zero velocity is set to be at the redshift of the C IV flux minimum. The fitted H I components are shown as coloured profiles with ticks marking the component velocity centre in the same colour, while the red profile represents the entire profile constructed from all the fitted components at $v \in [-150, +150]$ km s⁻¹. The data are shown in gray where the absorption is from blended metal lines or H I at velocities outside ± 150 km s⁻¹. Upper panel: Only the saturated H I Ly α is used in the Voigt profile fitting. The total $N_{\text{H I}}$ within ± 150 km s⁻¹ is 16.11 ± 0.20 . Lower panel: All the available high-order Lyman lines were fitted simultaneously. The H I absorption centred at $v \sim 0$ km s⁻¹ becomes unsaturated at Ly μ , revealing its 3-component nature. The total $N_{\text{H I}}$ within ± 150 km s⁻¹ is 17.28 ± 0.01 , which is 1.17 dex larger than the Ly α -only fit.

be $z > 1.98$. With an intervening Lyman limit system, the lowest redshift bound increases, as listed in the 3rd column of Table 1. Note that if $N_{\text{H I}}$ is high enough to show a damping wing, Ly α line alone is enough to estimate a robust $N_{\text{H I}}$. We also note that well-resolved unsaturated H I Ly α components do not require a high-order Lyman line to determine the line parameter, especially for high-S/N spectra we have used in this study. For relatively clean, unsaturated H I Ly α , the column density estimates are reliable at $\log N_{\text{H I}} \leq 14.3$.

However, the determination of the H I column density is not always straightforward. Even if several of the Lyman series lines are accessible, they are not always useful because of blending with lower redshift Ly α . At $z \gg 3$, line blending is so severe that most high-order lines become blended with the lower- z Ly α forest. Also, because of the higher absorption line density, the continuum level is uncertain. At $z < 2.5$, line blending becomes less problematic, but at lower redshifts the number of available high-order Lyman lines in

optical spectra also decreases. A further complication may occur in high redshift QSOs, when there are systems with $\log N_{\text{H I}} \geq 17.2$ in the observed spectrum. Since these have significant Lyman continuum absorption at the rest-frame wavelength $< 912 \text{ \AA}$ and decrease the flux significantly, the higher order Lyman lines in the system of interest may not be measurable in that region.

Another difficulty which strongly affects the analysis of saturated lines is uncertainties in the zero level in the data (Kim et al. 2007). In particular, at short wavelengths in UVES data, the true zero level offset could be a few percent of the local continuum. If the true zero is above the adopted one, then the fitting program attempts to put in many unsaturated components. If the true zero is below the adopted one, then the criterion for a satisfactory fit may never be satisfied. The zero level for each spectral region can be treated as a free parameter in VPFIT, so this option was used if appropriate.

For $\log N_{\text{H I}} \sim 16.5$ and $b = 30 \text{ km s}^{-1}$ (a typical line width of the Ly α forest), the Lyman lines start to become unsaturated at higher order than Ly η (926.23 \AA). The residual central intensity of Ly θ (923.15 \AA) is then $\sim 4\%$ of the continuum, and for Ly ι (920.96 \AA), $\sim 10\%$. We have found empirically that a fairly robust $N_{\text{H I}}$ can be obtained within 0.1 dex if both Ly β and Ly γ are included in the fit and if $\log N_{\text{H I}} \leq 17.0$. Even if only Ly α and Ly β are available, the $N_{\text{H I}}$ obtained assuming a single component is usually within 0.1–0.2 dex. However, the difference could become larger if a saturated line reveals several components at higher orders than Ly β . About 31% of the saturated Ly α in our H I+C IV sample breaks into several components in Ly β . About 39% of the saturated Ly α breaks into several weaker components at higher orders than Ly β .

Figure 2 illustrates the importance of incorporating high-order lines in the profile fitting procedure and the difficulty in obtaining reliable fit parameters. As the S/N in the Ly α region is about 160 per pixel, it is easy to recognise even by eye that a single-component fit for the saturated core does not match the observed left wing profile. For such a fit the normalised $\chi^2 \sim 6.1$. There are two saturated H I absorbers, the $z = 2.727849$ absorber toward PKS2126–158 and the $z = 2.328908$ absorber toward HE1347–2457, for which a low-S/N in the available higher-order regions makes it difficult to estimate the saturated line parameters reliably. For the former case, depending on a one- or two-component structure at $v = 11 \text{ km s}^{-1}$, the resultant column density can be differ by 0.38 dex. For the $z = 2.328908$ absorber toward HE1347–2457, the saturated component at $v = 14 \text{ km s}^{-1}$ could have a $N_{\text{H I}}$ difference by 0.72 dex, depending on the b value. With no significant improvement in the normalised χ^2 value, we took the one-component fit and the smaller- b fit, respectively, but increased their error to include the error range by the alternative fit. We note that lines in the absorption wings tend to have a larger error in z , b and N .

In our H I+C IV sample, we included only those with a well-measured $N_{\text{H I}}$ obtained by including high-order lines or from unsaturated Ly α . When Ly α is saturated and no constraint could be obtained from Ly β or other higher-order lines because of blending, that H I+C IV pair was excluded. However, this resulted in the exclusion of only $\sim 2\%$ of all the H I+C IV pairs. Saturated C IV components associated with the forest H I are much less common. There are only

two saturated C IV components in our sample, and both of these are in systems with $\log N_{\text{H I}} \geq 17$. These are included only as lower limits for illustration purposes, but excluded from the actual analysis.

3.3 Detection of weak C IV lines

The detection of weak lines depends critically on the local S/N and the absorption line width b . A weak, narrow line is more easily recognised than a strong, broad line. To construct a robust H I+C IV sample, we selected a C IV component only when the stronger doublet C IV $\lambda 1548$ is detected at the $\geq 3\sigma$ level. Following the procedure described in Sembach et al. (1991), a standard deviation, 1 r.m.s. (1σ), was measured in the nearby, unabsorbed continuum region. When a weak C IV line was detected, the equivalent width (EW) of C IV $\lambda 1548$ was estimated over the region which the line profile falls, including the $\pm 0.5\sigma$ continuum fitting errors. This EW with the continuum errors is then compared to the 1σ continuum EW integrated over the same wavelength range to obtain the detection significance.

For $S/N \sim 100$, the C IV detection limit at 3σ is $\log N_{\text{C IV}} \sim 12.0$. In a similar way, a rough detection limit of H I at 3σ is $\log N_{\text{H I}} \sim 12.5$ for $S/N \sim 60$. All of our 21 UVES spectra were included in the high- z C IV study by D’Odorico et al. (2010). In our analysed redshift range, about 5% of the C IV absorbers are not reported in D’Odorico et al. (2010). Most of these are weak C IV at $\sim 3\sigma$. The discrepancies occur mainly when one line of the doublet is blended with other lines or weak telluric features, though in some cases misidentification of C IV could be responsible. We included the border-line detections in our H I+C IV sample, as there are so few of them that the scientific results and conclusions are unaffected.

4 WORKING DEFINITION OF A SYSTEM AND A CLUMP DESCRIBING C IV ABSORBERS

Various terms such as clouds, groups, clumps and systems have been used to describe QSO absorption features. These terms are often used interchangeably. Physically, it becomes meaningful to associate H I with C IV only if an effect on H I triggers a consequence on C IV and vice versa. However, there is no independent way to recognise this physical connection from the spectroscopic data alone. Even though the H I gas and the C IV gas are very far in the real space, their lines could be found to be very close in the redshift space in QSO spectra due to the bulk motions and the peculiar velocity (Rauch et al. 1997).

To describe our H I+C IV sample more clearly for this study, we re-define two terms commonly used in the literature, *systems* and *clumps*. Our definitions are solely based on the *profile shapes*, assuming that a similar velocity structure between H I and C IV is produced by similar underlying physical processes. Other terms such as an absorber, a component or a line are used loosely having a similar meaning as in the literature. We illustrate these working definitions in Figs. 3 and 4, which shows the normalised flux vs relative velocity of C IV systems. The top panel displays other associated metal species such as Si IV, N V or O VI. When no

clear metal species other than C IV are detected in the observed wavelength range, Si IV $\lambda 1393$ is shown. The name of the QSO and the redshift of the C IV system listed on top are colour-coded according to $N_{\text{C IV}}$ compared to $N_{\text{H I}}$ as explained in Section 5.1. Note that even though we showed only a portion of fitted spectra in Figs. 3 and 4 for clarity, we have fitted almost entire spectra to obtain a reliable $N_{\text{H I}}$ and $N_{\text{C IV}}$, as explained in Section 3.

4.1 Components

A *component* is the most basic and simplest unit to describe absorption profiles. However, the component structure determined by fitting Voigt profiles is not unique and is strongly dependent on the spectral resolution and S/N (Kim et al. 2013; Boksenberg & Sargent 2015). So, for all but the simplest line profiles, the component structure is not well-determined. In this work, the components are strictly referred to the VPFIT profile fitting results.

Since VPFIT profile fitting depends on the continuum and S/N, a slightly different velocity centroid can be obtained for H I and C IV, even if both are produced in the same absorbing gas. Here, depending on the velocity difference, the presence of close components and the detection significance, H I+C IV component pairs were classified into well-aligned and reasonably-aligned components.

Well-aligned components refer to the H I and C IV pairs when their velocity centroid differs by $\leq 5 \text{ km s}^{-1}$ for a unsaturated, single-component C IV and both are relatively clean and well-measured. The H I+C IV component pairs marked with a thick blue tick in the upper-middle panel of Fig. 3 are a good example of well-aligned components.

Reasonably-aligned components refer to the ones which also have a velocity difference at $\leq 5 \text{ km s}^{-1}$, but if nearby H I components make the line parameter of the aligned H I less reliable or if a C IV is located in a low-S/N region.

This classification is only applied for a H I+C IV component pair which is isolated or separable from other nearby H I and C IV. When several C IV components are associated with a H I absorption with a smaller number of H I components, e.g. the C IV components at $v \sim 0$ and $\sim 60 \text{ km s}^{-1}$ in the upper-middle panel of Fig. 3, there is no unambiguous way to assign each C IV component to H I. In this case, regardless of the small velocity difference between H I+C IV pairs, they are not classified to be aligned.

Considering that the wavelength calibration of UVES and HIRES spectra is usually better than $\sim 1 \text{ km s}^{-1}$, this arbitrary choice of 5 km s^{-1} is likely to be too generous for strong and narrow components, and is reasonable for weak and broad components. Our sample consists of 762 H I components and 628 C IV components. Only 6% of the C IV components (38/628) are well-aligned. Reasonably-aligned C IV components are similar at $\sim 6\%$ (39/628).

4.2 Systems

The C IV *system* is defined by all the C IV components at $v \in [-150, +150] \text{ km s}^{-1}$ centred at the C IV flux minimum of a single or a group of several, closely-located C IV components. The redshift of a C IV system defined in this way is not necessarily the redshift of the strongest C IV component, since a strongest component has sometimes a broader

line width. In some cases, a continuous C IV absorption profile extends beyond $\pm 150 \text{ km s}^{-1}$ or a C IV absorption is outside the velocity range, but with a separation less than 100 km s^{-1} . In such cases, the integrated velocity range is extended by a 100 km s^{-1} step to include these C IV. If necessary, a new zero velocity is defined to be at a C IV flux minimum including the newly-added C IV. The exactly same velocity range is used to assign *associated* H I or other metal components.

The upper-left panel in Fig. 3 shows a common C IV system. For about 80% of our sample, the C IV profile is rather simple and associated with saturated H I. The upper-middle panel presents a rare C IV system, in which the C IV absorption is stronger than the one of typical H I absorbers having a similar $N_{\text{H I}}$. These are the high-metallicity absorbers described by Schaye, Carswell & Kim (2007). As the C IV absorption continues at $v > +150 \text{ km s}^{-1}$, the integrated velocity range is extended to $v \in [-150, +250] \text{ km s}^{-1}$. In the upper-right panel of Fig. 3, an additional C IV absorption occurs beyond the $\pm 150 \text{ km s}^{-1}$ range. The separation between the wavelengths of the distinct C IV profile wings to recover to the normalised C IV flux of $F_{\text{C IV}} \sim 1$ is less than 100 km s^{-1} . Therefore, these C IV absorptions are combined as a single C IV system defined at $v \in [-250, +150] \text{ km s}^{-1}$.

This working definition of the C IV system does not require that a C IV centroid should coincide with a H I centroid. Moreover, the C IV system defined this way often includes nearby H I components clearly associated with no C IV. This definition is in fact more closely related to the *volume-averaged* quantities commonly used in numerical simulations. Note that a conventional definition of a C IV system in the literature would refer to a group of H I and C IV absorption features seemingly associated in the velocity space, but excluding any C IV-free H I components. We label H I and C IV column densities of a system as the *integrated* $N_{\text{H I}}$ and $N_{\text{C IV}}$, or $N_{\text{H I, sys}}$ and $N_{\text{C IV, sys}}$. When we want to emphasize the given integrated velocity range, we use $N_{\text{H I}}(\pm 150)$ and $N_{\text{C IV}}(\pm 150)$.

On the face value, the fixed velocity range of $\pm 150 \text{ km s}^{-1}$ to define a system could be considered rather arbitrary. This range was chosen on the basis of several observational findings. Studies of close QSO pairs have found a strong C IV clustering signal within $\sim 200 \text{ km s}^{-1}$, which might indicate the outflow velocity could be less than $\sim 200 \text{ km s}^{-1}$ (Rauch et al. 2005). A significant clustering signal of H I is also found at a transverse velocity separation at $\sim 500 \text{ km s}^{-1}$ (D’Odorico et al. 2006). The average velocity dispersions of high- z galaxies are $\langle \sigma \rangle \sim 120 \text{ km s}^{-1}$ (Erb et al. 2006). As shown in Section 5.1, the integrated $N_{\text{H I}}-N_{\text{C IV}}$ relation depends on the integrated velocity range when it is small. However, as the integrated velocity range becomes $\geq \pm 100 \text{ km s}^{-1}$, the integrated $N_{\text{H I}}-N_{\text{C IV}}$ relation converges.

4.3 Clumps

Closely-located C IV components often show visibly distinct, separable absorption features. When the absorption wing of visibly separable C IV profiles recovers to have a normalised flux $F_{\text{C IV}} = 1$ and a closest C IV absorption wing starts at $\geq 5 \text{ km s}^{-1}$ away, this distinct absorption feature is termed as a *clump*. As with the C IV system, all the H I compo-

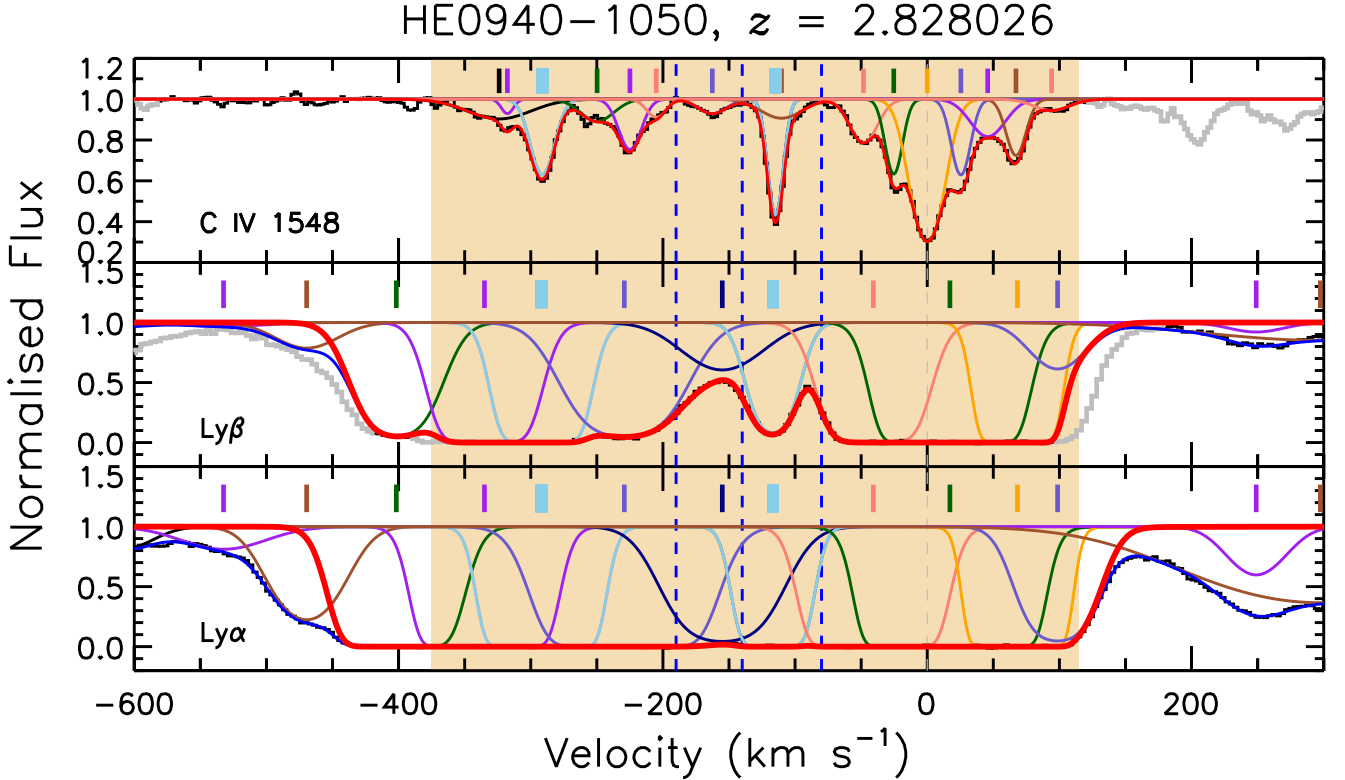


Figure 4. The velocity plot of the $z = 2.828026$ C IV system toward HE0940-1050, defined at $v \in [-450, +250]$ km s $^{-1}$. All the symbols are the same as in Figs. 2 and 3. The three blue dashed, vertical lines delineate the relative velocity at -190 , -140 and $+80$ km s $^{-1}$, where the normalised C IV flux F_{CIV} becomes ~ 1 . Thick sky-blue ticks indicate the reasonably-aligned H I + C IV component pairs. See the text for details.

nents within the C IV clump velocity range are assigned to that clump. Even when a H I component exists just outside the clump velocity range, it is not extended to include this nearby H I component. Fortunately, such H I components are usually weak so that the clump H I column density, $N_{\text{HI,cl}}$, does not increase significantly even if they are included. If no H I exists within the clump velocity range, the velocity range is extended to include a nearby H I component based on both H I and C IV absorption profile shapes. A clump can consist of a single component or multiple components.

In the upper-left panel of Fig. 3, the single C IV absorption profile wings recover to the normalised C IV flux of 1 at $v \in [-60, +25]$ km s $^{-1}$. As 3 H I components exist in the C IV clump velocity range, this C IV system consists of one C IV clump. The clump column density of H I and C IV is integrated over the clump velocity range. In the upper-right panel, the two distinct C IV absorptions span at $v \in [-240, -170]$ and $[-80, +20]$ km s $^{-1}$. As only H I components within each clump velocity range are included to define $N_{\text{HI,cl}}$, the H I component at $v \sim -109$ km s $^{-1}$ is not included in either two clump H I column densities.

The lower panels of Fig. 3 present three C IV systems for which defining a clump is not straightforward. In the lower-left panel, there exists a H I component in each cleanly-defined C IV clump velocity range, even though both H I and C IV are fitted independently. Therefore, the system is classified to consist of 2 clumps. On the other hand, in the lower-middle panel, no H I component exists within the C IV

clump velocity range at $v \in [-25, +25]$ km s $^{-1}$. The closest H I component is at 4 km s $^{-1}$ away at $v = +29$ km s $^{-1}$. However, the C IV absorption is more likely to be associated with the H I absorption at $v = -58$ km s $^{-1}$. The H I profile clearly reveals a separation of two distinct H I absorptions at $v \sim 20$ km s $^{-1}$ and the C IV absorption occurs at $v < 20$ km s $^{-1}$. Therefore, the clump velocity range is defined as $v \in [-100, +25]$ km s $^{-1}$ to include only H I at $v = -58$ km s $^{-1}$.

If the same reasoning is applied, in the lower-right panel, the broad C IV absorption at $v = +45$ km s $^{-1}$ should be assigned to the H I at $v = +83$ km s $^{-1}$, the strongest H I component. However, since 2 H I components exist in the clump velocity range at $v \in [-55, +75]$ km s $^{-1}$, we strictly applied for the clump criterion without including the H I component at $v = +83$ km s $^{-1}$. Fortunately, only about 5% of the clumps are ambiguous for reasons similar to the last two examples.

Figure 4 illustrates another example of a clump. It shows a velocity plot of one of the most complicated C IV systems at $z = 2.828026$ toward HE0940-1050, defined at $v \in [-450, +250]$ km s $^{-1}$. Considering the C IV profile only at $v \in [-375, +115]$ km s $^{-1}$, the C IV flux is recovered to the normalised flux of $F_{\text{CIV}} = 1$ at $v = -190$ km s $^{-1}$, but the left wing of the C IV profile due to the $v = -163$ km s $^{-1}$ component does not allow the $F_{\text{CIV}} \sim 1$ region more than 5 km s $^{-1}$. The normalised flux does not reach to $F_{\text{CIV}} = 1$ at $v = -140$ and -80 km s $^{-1}$. Therefore, this system con-

sists of only one clump. Most of high- $N_{\text{H I}}$ absorbers have a continuous C IV absorption profile spanning over several hundred km s^{-1} similar to the shown example, consisting of only 1 clump.

Unfortunately, the H I component structure is not as well-determined as the C IV due to the larger H I thermal width and the non-uniqueness of the Voigt profile fitting. Therefore, assigning H I components to a C IV clump in a smaller velocity range than the system is not necessarily robust. In addition, finding a velocity at which the C IV flux recovers to a normalized flux $F_{\text{C IV}} = 1$ is not always reliable, depending on the local S/N and the goodness of the continuum placement.

Due to these uncertainties, we used one supplementary definition to study C IV clumps, a $\text{Ly}\alpha\beta$ clump. If a normalised C IV flux becomes at $F_{\text{C IV}} \geq 0.98$ at a relative velocity v and both H I $\text{Ly}\alpha$ and $\text{Ly}\beta$ absorption profiles are also clearly breakable at the similar velocity, this distinct absorption feature is termed as a $\text{Ly}\alpha\beta$ clump. The $\text{Ly}\alpha\beta$ clump is defined only in terms of the profile shape and is closest to the *conventional* C IV system commonly used in the literature.

In the upper-left panel of Fig. 3, the $\text{Ly}\alpha$ and $\text{Ly}\beta$ profiles show a smooth H I absorption at $v \in [-80, +200] \text{ km s}^{-1}$, without displaying any distinct component structure. The H I component at $v = +55 \text{ km s}^{-1}$ becomes distinguishable only at $\text{Ly}\gamma$. Therefore, even though the H I at $v = +55 \text{ km s}^{-1}$ does not associated with the C IV directly, all the H I at $v \in [-80, +200] \text{ km s}^{-1}$ are included for the H I column density of this $\text{Ly}\alpha\beta$ clump, $N_{\text{H I}, \alpha\beta}$. Similarly, both $\text{Ly}\alpha$ and $\text{Ly}\beta$ profiles in the lower-left panel display a smooth absorption at $v \in [-200, +40] \text{ km s}^{-1}$, while two distinct C IV absorptions are separated at $v \sim 50 \text{ km s}^{-1}$. Therefore, this system contains only one $\text{Ly}\alpha\beta$ clump at $v \in [-200, +40] \text{ km s}^{-1}$. In Fig. 4, within the system velocity range $v \in [-450, +150] \text{ km s}^{-1}$, the C IV absorption flux becomes at $F_{\text{C IV}} \geq 0.98$ at $v \sim -375, -190, -140, -80$ and $+115 \text{ km s}^{-1}$, while the H I profile from $\text{Ly}\alpha$ and $\text{Ly}\beta$ breaks at $v \sim -450, -375, -250, -155, -150, -85$ and $+140 \text{ km s}^{-1}$. Therefore, this system consists of 3 $\text{Ly}\alpha\beta$ clumps at $v \in [-375, -140]$, $[-140, -80]$ and $[-80, +115] \text{ km s}^{-1}$.

$\text{Ly}\alpha\beta$ clumps are analysed only in Section 5.4. In this work, clumps refer only to a clump defined by a velocity range of a distinct C IV absorption.

In this working definition, our H I+C IV sample consists of 183 C IV systems, 227 C IV clumps, 38 well-aligned and 39 reasonably-aligned H I+C IV component pairs at $1.7 < z < 3.3$. Figure 5 shows their redshift distribution.

Tables 2 and 3 list the integrated column densities of H I and C IV of the first few C IV systems and clumps, respectively, along with their QSO names, the system redshift and the velocity range integrated over. The full tables are published electronically. The 7th column of Table 2 is the C IV-profile weighted line width, calculated using Eq. (5) of Sembach & Savage (1992). Its mean value is $< \sigma_{\text{C IV}} > = 30.2 \text{ km s}^{-1}$.

The 6th column of Table 3 indicates whether a clump is well-defined or uncertain due to the absence of H I in the clump velocity range. The last columns of Tables 2 and 3 note any associated Si IV, O VI and N V. Gener-

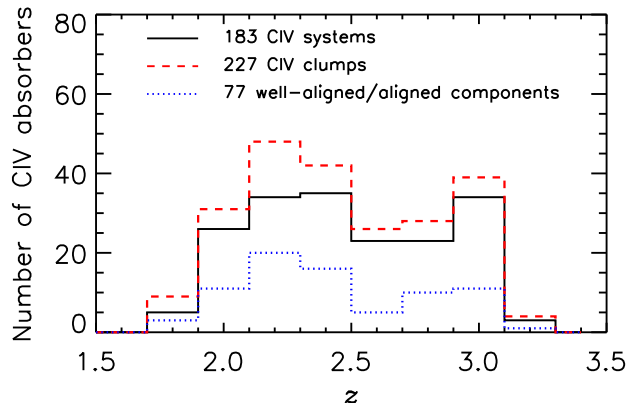


Figure 5. The redshift distribution of 183 C IV systems (black solid line), 227 C IV clumps (red dashed line) and 77 well-aligned/reasonably-aligned H I+C IV components (blue dotted line). Since saturated H I lines at $z < 1.98$ are excluded in the sample except toward J2233–606 due to their highly uncertain $N_{\text{H I}}$, the number of the C IV systems decreases sharply.

ally, C IV systems with higher $N_{\text{H I}, \text{sys}}$ are likely to be associated with more metal species (Simcoe et al. 2004; Boksenberg & Sargent 2015). On the other hand, C IV systems without Si IV are likely to be associated with no other ions, and only rarely with N V or O VI (Carswell et al. 2002; Schaye et al. 2007).

Table 4 lists the individual fitted line parameters of the two C IV systems over an integrated velocity range. All the fitted parameters for each C IV system and its velocity plot are published electronically. The format of the velocity plot is the same as in Figs. 2, 3 and 4, with the well-aligned (reasonably-aligned) H I+C IV components marked with thick blue (sky-blue) ticks. We stress that we blindly include only the fitted lines within the integrated velocity range and show only selected transitions for simplicity and clarity, even though we have fitted almost the entire spectrum. Note that we do not use the line parameters of metal ions other than C IV in this study, except to check whether a C IV system is associated with other metals. Therefore, only the line parameters of Si IV are listed in Table 4 to show a Si IV profile aligned with C IV. The entire fitted line lists will be published online in near future.

5 THE $N_{\text{H I}}-N_{\text{C IV}}$ RELATION OF C IV SYSTEMS AND CLUMPS

5.1 The integrated $N_{\text{H I}}-N_{\text{C IV}}$ relation for C IV systems

Figure 6 shows the integrated $N_{\text{H I}}-N_{\text{C IV}}$ relation for a fixed velocity range of $v \in [-150, +150] \text{ km s}^{-1}$. Integrated column densities are obtained from adding up *blindly* all the H I and C IV components over a given velocity ranges for each system. The associated errors are calculated using the standard error propagation for addition assuming uncorrelated errors as follows, for each i -th component $\log N_i + \sigma(\log N_i) = y_i + \sigma(y_i)$:

Table 2. The integrated column densities of the C IV systems at the $v = \pm 150 \text{ km s}^{-1}$ range. Only the beginning of the entire table is shown. The full version of this table is available electronically on the MNRAS website.

QSO	z_{abs}	class ^a	$[v_1, v_2]^b$ (km s^{-1})	$\log N_{\text{H I, sys}}^c$	$\log N_{\text{C IV, sys}}^c$	$\Delta_{\text{C IV, sys}}$ (km s^{-1})	Other ions ^d
Q0055–269	3.256200	2		15.33 ± 0.02	13.58 ± 0.05	36.0	Si IV, O VI
Q0055–269	3.248119	2	$[-150, +250]$	15.44 ± 0.01	13.04 ± 0.03	77.8	
Q0055–269	3.190942	1	$[-150, +350]$	15.67 ± 0.03	14.58 ± 0.03	102.3	Si IV
Q0055–269	3.095658	2		15.06 ± 0.06	12.85 ± 0.05	6.9	
Q0055–269	3.085889	2		15.37 ± 0.02	13.16 ± 0.08	11.2	Si IV
Q0055–269	3.038793	2	$[-250, +150]$	15.12 ± 0.03	13.00 ± 0.02	78.4	
Q0055–269	3.004992	2		15.23 ± 0.03	12.81 ± 0.03	13.8	blends
Q0055–269	2.950571	2	$[-250, +150]$	15.71 ± 0.03	13.87 ± 0.03	65.9	Si IV
Q0055–269	2.945250	3		16.74 ± 0.02	12.91 ± 0.02	14.1	Si IV
Q0055–269	2.913867	2		15.30 ± 0.02	12.82 ± 0.03	19.0	
Q0055–269	2.895563	2		15.48 ± 0.06	12.98 ± 0.02	15.4	blends
Q0055–269	2.744091	2		15.43 ± 0.04	13.12 ± 0.04	38.0	
Q0055–269	2.705788	2		14.97 ± 0.13	12.54 ± 0.03	11.4	

^a Class ‘1’, ‘2’ and ‘3’ refer to higher-, normal and lower- $N_{\text{C IV}}$ systems, as shown in red, black and sky-blue filled circles in Fig. 9. See Section 5.2 for details.

^b Listed only when the velocity range has to be extended from the default $\pm 150 \text{ km s}^{-1}$ velocity range.

^c The associated error of the integrated column densities was calculated using the standard, independent error propagation method when adding up the column densities. This is *not* the error obtained using the summed column densities option in VPFIT, which is usually much smaller.

^d Only Si IV, O VI and N V are listed. If Si IV is not detected and O VI and N V are blended or not detected, the entry is left blank. When Si IV is blended and N V and O VI are also blended or not detected, the entry is noted as ‘blends’. The entry ‘out of range’ indicates that all of Si IV, O VI and N V are out of the observed wavelength range. A system including a saturated C IV is noted as ‘saturated C IV’.

Table 3. The integrated column densities of C IV clumps. Only the beginning of the entire table is shown. The full version of this table is available electronically on the MNRAS website.

QSO	z_{abs}	$[v_1, v_2]$ (km s^{-1})	$\log N_{\text{H I, cl}}^a$	$\log N_{\text{C IV, cl}}^a$	Class ^b	Other ions ^c
Q0055–269	3.256200	$[-40, +100]$	15.31 ± 0.02	13.58 ± 0.05		Si IV, O VI
Q0055–269	3.248119	$[-15, 45]$	13.95 ± 0.08	12.80 ± 0.03	uncertain	
Q0055–269	3.248119	$[+125, +200]$	15.26 ± 0.02	12.67 ± 0.05		
Q0055–269	3.190942	$[-100, +300]$	15.67 ± 0.03	14.58 ± 0.03		Si IV
Q0055–269	3.095658	$[-20, +20]$	15.06 ± 0.06	12.85 ± 0.05		
Q0055–269	3.085889	$[-25, +30]$	15.36 ± 0.02	13.16 ± 0.08		Si IV
Q0055–269	3.038793	$[-210, -170]$	14.23 ± 0.03	12.25 ± 0.07		
Q0055–269	3.038793	$[-160, -80]$	14.51 ± 0.03	12.45 ± 0.06		
Q0055–269	3.038793	$[-25, +30]$	14.70 ± 0.06	12.73 ± 0.03		
Q0055–269	3.004992	$[-30, +30]$	15.21 ± 0.03	12.81 ± 0.03		blends
Q0055–269	2.950571	$[-165, +120]$	15.71 ± 0.03	13.87 ± 0.03		Si IV
Q0055–269	2.945250	$[-30, +30]$	16.74 ± 0.02	12.91 ± 0.02		Si IV
Q0055–269	2.913867	$[-40, +40]$	15.21 ± 0.03	12.82 ± 0.03		
Q0055–269	2.895563	$[-35, +35]$	15.46 ± 0.06	12.98 ± 0.02		blends
Q0055–269	2.744091	$[-135, +30]$	15.43 ± 0.04	13.12 ± 0.04		
Q0055–269	2.705788	$[-30, +30]$	14.96 ± 0.13	12.54 ± 0.03		

^a Same as in Footnote ‘c’ in Table 2.

^b The blank entry indicates a well-defined clump. The ‘uncertain’ entry notes a uncertain clump due to the absence of H I in the velocity range of a C IV absorption or due to the ambiguous association of H I and C IV. The ‘nearby H I’ entry means that there exists a H I component within 10 km s^{-1} from either velocity bound. The ‘saturated C IV’ entry notes that a clump contains a saturated C IV.

^c Same as in Footnote ‘d’ in Table 2.

$$N_{\text{tot}} = \sum_i 10^{y_i},$$

which leads to

$$\sigma(N_{\text{tot}}) = \sqrt{\sum_i \sigma(y_i) \times 10^{y_i} / 0.434},$$

$$\log N_{\text{tot}} + \sigma(\log N_{\text{tot}}) = \log(N_{\text{tot}}) + 0.434 \times \frac{\sigma(N_{\text{tot}})}{N_{\text{tot}}}. \quad (1)$$

This is usually dominated by a few components with a large error. Therefore, when a system contains such com-

Table 4. The line parameters of individual C IV systems. Only the beginning of the entire table is shown. The full version of this table is available electronically on the MNRAS website.

#	Ion	v (km s ⁻¹)	z	b (km s ⁻¹)	log N
Q0055-269		$z = 3.256200$	[-150, +150] km s ⁻¹		
1	H I	-136 ± 12	3.254260	10.6 ± 4.7	12.04 ± 0.20
2	H I	-71 ± 17	3.255193	37.9 ± 3.3	13.73 ± 0.06
3	Si IV	-25 ± 16	3.255850	10.6 ± 5.8	11.80 ± 0.18
4	C IV	-18 ± 13	3.255943	11.9 ± 2.9	12.87 ± 0.14
5	Si IV	-1 ± 6	3.256186	9.7 ± 2.1	12.17 ± 0.08
6	C IV	0 ± 5	3.256200	9.5 ± 1.3	13.06 ± 0.09
7	H I	16 ± 2	3.256422	39.1 ± 0.9	15.31 ± 0.02
8	C IV	29 ± 10	3.256616	10.0 ± 3.3	12.57 ± 0.16
9	Si IV	46 ± 17	3.256858	22.0 ± 6.5	11.99 ± 0.10
10	C IV	52 ± 6	3.256940	13.0 ± 2.3	12.99 ± 0.07
11	C IV	82 ± 4	3.257366	9.7 ± 1.3	12.73 ± 0.04
12	H I	93 ± 7	3.257523	18.1 ± 1.6	13.51 ± 0.07
13	H I	145 ± 5	3.258263	26.1 ± 2.5	13.14 ± 0.04
Q0055-269,		$z = 3.248119$,	[-150, +250] km s ⁻¹		
1	H I	-144 ± 32	3.246077	26.9 ± 7.2	12.70 ± 0.20
2	H I	-64 ± 8	3.247206	41.2 ± 2.3	14.43 ± 0.02
3	H I	-11 ± 6	3.247961	17.7 ± 2.3	13.95 ± 0.08
4	C IV	0 ± 2	3.248119	4.0 ± 0.9	12.50 ± 0.04
5	C IV	23 ± 4	3.248447	9.8 ± 1.7	12.49 ± 0.05
6	H I	61 ± 4	3.248988	44.7 ± 2.2	14.77 ± 0.02
7	H I	161 ± 2	3.250407	31.1 ± 0.5	15.26 ± 0.02
8	C IV	166 ± 10	3.250474	23.8 ± 3.4	12.67 ± 0.05

ponents, the error is often over-estimated compared to the one obtained by using the summed column densities option in VPFIT. Since the VPFIT error is only a fit error without a continuum fitting uncertainty in the way usually adopted in the studies of the Milky Way interstellar medium, e.g. Sembach et al. (1991) and since our fit error is already small, mostly with less than 0.05 dex, we decided to use this standard error for addition. Keep in mind that the column density defined this way is similar to the volume-averaged column density. We also note that the integrated column density is in general measured more reliably than $N_{\text{H I}}$ and b of individual components (see Sections 3.1 and 3.2).

Of the 183 C IV systems, 64 are Si IV-enriched, 103 are Si IV-free ($\log N_{\text{Si IV}} \leq 11.5$) and 16 have blended or uncertain Si IV systems. As expected, those with extended velocity range marked with open symbols tend to be associated with systems showing higher- $N_{\text{C IV, sys}}$ and Si IV, as stronger C IV in general consists of multiple components spread over a larger velocity range and is associated with other ions. Otherwise, there is no strong segregation on the $N_{\text{H I, sys}} - N_{\text{C IV, sys}}$ plane. Therefore, no distinction is made in the further analysis between the C IV systems integrated over the $\pm 150 \text{ km s}^{-1}$ and extended velocity ranges.

The data points of LLSs/sub-DLAs/DLAs at $1.7 < z < 3.3$ are compiled from literature. Any duplicated absorber from the literature was discarded in favour of our own measurements. In studies on sub-DLAs and DLAs, C IV is not an ion of a main interest, therefore, not many measurements are available in the literature. Both $N_{\text{H I}}$ and $N_{\text{C IV}}$ taken from the literature do not meet our definition of a C IV system.

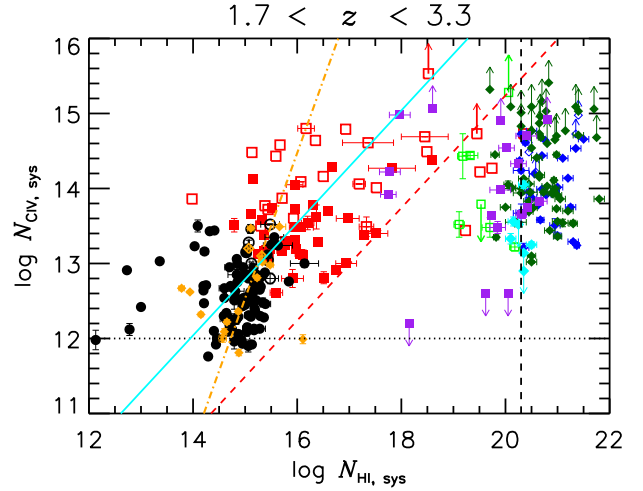


Figure 6. The integrated $N_{\text{H I}} - N_{\text{C IV}}$ relation including the LLSs/sub-DLAs/DLAs. Filled and open symbols represent the C IV systems integrated over $\pm 150 \text{ km s}^{-1}$ and the extended velocity ranges, respectively. Circles and red squares indicate C IV systems without associated Si IV and with Si IV, respectively, while orange diamonds represent systems whose Si IV region is blended. For LLSs/sub-DLAs/DLAs, the data are from (Prochaska et al. 2001, 2003, filled blue diamonds), (Dessauges-Zavadsky et al. 2003, open light green squares), (Fox et al. 2007b, filled dark green diamonds), (Pérout et al. 2007, open light green squares), (Penprase et al. 2010, filled cyan diamonds) and (Lehner et al. 2014, filled purple squares). Only errors larger than the symbol size are shown for clarity. The red dashed line delineates a $N_{\text{H I}} - N_{\text{C IV}}$ relation converted from the IGM median optical depth relation between H I and C IV estimated by Schaye et al. (2003), while the cyan solid line is the same relation with 20 times stronger $N_{\text{C IV}}$. See the text for details. The orange dot-dashed line is a robust, single power-law fit for systems at $\log N_{\text{H I, sys}} \in [14, 16]$: $\log N_{\text{C IV, sys}} = (-16.52 \pm 3.77) + (1.94 \pm 0.25) \times \log N_{\text{H I, sys}}$. The horizontal dotted line and the vertical dashed line note the “practical” C IV detection limit at $\log N_{\text{C IV}} = 12.0$ and the border line between sub-DLAs and DLAs at $\log N_{\text{H I}} = 20.3$. For any ambiguities, refer to the online, coloured version.

However, both values can be considered to be added up over the same extended velocity range, as including any typical forest H I absorbers near sub-DLAs and DLAs in a given velocity range has a negligible effect on their $N_{\text{H I}}$.

The red dashed line delineates a $N_{\text{H I}}$ and $N_{\text{C IV}}$ relation, $\log N_{\text{C IV}} \sim 0.75 \times \log N_{\text{H I}} + 0.24$. This was converted from the relation between the median H I and C IV optical depths ($\tau_{\text{H I, med}}$ and $\tau_{\text{C IV, med}}$) at $z \sim 3$: $\log \tau_{\text{C IV, med}} \sim 0.75 \times \log \tau_{\text{H I, med}} - 3.0$ at $\log \tau_{\text{H I, med}} \geq 0.1$ (Schaye et al. 2003). Converting an optical depth to a column density is not trivial and requires a b parameter. We assumed that the $\tau_{\text{H I, med}} - \log \tau_{\text{C IV, med}}$ relation holds on an optical depth at a line centre of H I and C IV, and assigned a single b value for H I and C IV as $b_{\text{H I}} = 25.8 \text{ km s}^{-1}$ and $b_{\text{C IV}} = 10.8 \text{ km s}^{-1}$, respectively. These b values are the median b value of H I and C IV in the analysed redshift range listed in Table 1.

The optical depth analysis uses all the H I absorption regardless of its association to C IV. On the other hand, the integrated $N_{\text{H I}} - N_{\text{C IV}}$ relation uses only for H I absorbers associated with C IV. This difference causes that the optical-depth-converted $N_{\text{H I}} - N_{\text{C IV}}$ relation is below most

data points in Fig. 6. The cyan line presents the same τ -converted $N_{\text{H I}}-N_{\text{C IV}}$ relation if $N_{\text{C IV}}$ is 20 times stronger. This proportionality constant of 20 is not based on any fit, but is chosen to match a majority of the data points at $\log N_{\text{H I, sys}} \in [14, 17]$. This implies that the median $\tau_{\text{C IV}}-\tau_{\text{H I}}$ relation samples the IGM gas having about 20 times lower C IV than the individually detected C IV-enriched gas.

There are three noticeable features in the integrated $N_{\text{H I}}-N_{\text{C IV}}$ relation:

1. At $N_{\text{C IV, sys}} \geq 12.8$, $N_{\text{H I, sys}}$ and $N_{\text{C IV, sys}}$ display a scatter plot, independent of $N_{\text{H I, sys}}$, even with a lack of C IV systems at $N_{\text{H I, sys}} \sim 18$ (Simcoe et al. 2004). Systems showing only a scatter on the $N_{\text{H I, sys}}-N_{\text{C IV, sys}}$ plane include most Si IV-enriched C IV systems shown in red filled/open squares including sub-DLAs and DLAs.

2. A majority of Si IV-free C IV systems at $\log N_{\text{C IV, sys}} \leq 13$ shown in filled and open circles follow a well-defined power-law relation between $N_{\text{H I, sys}}$ and $N_{\text{C IV, sys}}$, mostly concentrating at $\log N_{\text{H I, sys}} \sim 15$. The orange dot-dashed line is a robust, single power-law fit to Si IV-free systems at $\log N_{\text{H I, sys}} \in [14.0, 16.0]$: $\log N_{\text{C IV, sys}} = (-16.52 \pm 3.77) + (1.94 \pm 0.25) \times \log N_{\text{H I, sys}}$. This power-law is much steeper than from the optical depth analysis.

For all the C IV systems at $\log N_{\text{H I, sys}} \in [12, 22]$, $N_{\text{C IV, sys}}$ shows a steep increase at $\log N_{\text{H I, sys}} \in [14, 16]$ from the C IV detection limit, spanning ~ 2 dex at $N_{\text{H I, sys}} \sim 15$. Then, the relation becomes more or less flattened at $\log N_{\text{H I, sys}} \geq 16$, with a large scatter of ~ 2.5 dex. C IV systems in the $N_{\text{H I, sys}}-N_{\text{C IV, sys}}$ plane at $(N_{\text{H I, sys}}, N_{\text{C IV, sys}}) \sim (17-22, \leq 13)$ do exist, but are rare. It is clear that a single power law only describes the $N_{\text{H I, sys}}-N_{\text{C IV, sys}}$ relation over a short $N_{\text{H I, sys}}$ range, mainly for Si IV-free C IV systems.

3. There are a few outliers in the left and right sides of the orange dot-dashed line, especially apparent at $\log N_{\text{H I, sys}} \leq 14$. Despite a large scatter expected in $N_{\text{C IV, sys}}$ for any given $N_{\text{H I, sys}}$, hardly any C IV systems would be expected at $\log N_{\text{H I, sys}} \leq 14$, if naively extrapolated from the $N_{\text{H I, sys}}-N_{\text{C IV, sys}}$ relation displayed by most C IV systems. The systems at $\log N_{\text{H I, sys}} \leq 14$ belong to a class of absorbers named as high-metallicity absorbers extensively studied in Schaye et al. (2007). Their $N_{\text{C IV}}$ is much higher than typical C IV absorbers with a similar $N_{\text{H I}}$, leading to a higher metallicity than the typical H I forest. Schaye et al. (2007) argue that high-metallicity absorbers are a transient object transporting recently metal-enriched gas from galaxies into the IGM.

There also exist systems at the right side of the orange dot-dashed line. These systems have lower $N_{\text{C IV, sys}}$ than other typical systems having the same $N_{\text{H I, sys}}$. There is even a system at $(\log N_{\text{H I, sys}}, \log N_{\text{C IV, sys}}) \sim (16, 12)$, for which a higher $\log N_{\text{C IV, sys}}$ is expected. This system is the $z = 2.326893$ absorber toward Q0109-3518. The saturated H I Ly α consists of two H I components separated by $\sim 45 \text{ km s}^{-1}$. A weak C IV is associated with a stronger H I with C III, Si III and possibly Si IV, while a weaker H I component at $v \sim +45 \text{ km s}^{-1}$ is associated with C III and Si III, but not with C IV. Even though two H I components are very close in the velocity space, their physical condition seems fairly different from each other and from typical forest absorbers, either due to the different ionising field, gas density or metallicity.

5.2 A fit to the $N_{\text{H I, sys}}-N_{\text{C IV, sys}}$ relation

The left panel of Fig. 7 shows a more detailed version of Fig. 6. Filled circles, open circles and blue open squares represent C IV systems having a single-component C IV, a 2-or-3-component C IV and a multi-component C IV. As expected, most single-component C IV systems have a lower $N_{\text{C IV, sys}}$ and do not have associated Si IV. Multi-component systems have a higher $N_{\text{C IV, sys}}$ and are associated with Si IV. While a single power-law fit adequately describes at the limited $N_{\text{H I, sys}}$ range, a different fitting function is required for the entire $N_{\text{H I, sys}}$ range.

Hydrodynamic simulations including galactic winds as a primary IGM metal enrichment mechanism predict that metallicities increase rapidly with over-densities up to a critical overdensity, then flatten above this critical overdensity (Aguirre et al. 2001a; Oppenheimer et al. 2012; Bordoloi et al. 2014). The slope of the metallicity-overdensity relation depends on wind speed, wind formation epoch and star formation rate in the parents galaxies. Metallicities and overdensities can be translated into $N_{\text{C IV, sys}}$ and $N_{\text{H I, sys}}$ in terms of observations, as both observational quantities are similar to volume-averaged quantities. Based on these theoretical predictions, we adopted a simple rectangular hyperbola fitting function to describe the $N_{\text{H I, sys}}-N_{\text{C IV, sys}}$ relation:

$$\log N_{\text{C IV, sys}} = \left[\frac{C_1}{\log N_{\text{H I, sys}} + C_2} \right] + C_3. \quad (2)$$

To minimise the effect of a large scatter in $N_{\text{C IV, sys}}$ at a given $N_{\text{H I, sys}}$, we take a following approach:

1. We pre-selected the C IV systems having $\log N_{\text{H I, sys}} \leq 18.0$ and $\log N_{\text{C IV, sys}} \leq 14.5$ or having $\log N_{\text{H I, sys}} \geq 18.0$ and $\log N_{\text{C IV, sys}} \geq 14.0$. The C IV systems with an lower limit on $N_{\text{C IV, sys}}$ were excluded.

2. The selected H I+C IV pairs were binned at the $N_{\text{C IV, sys}}$ binsize of 0.4 at $\log N_{\text{C IV, sys}} \in [11.9, 14.3]$, where $N_{\text{H I, sys}}$ roughly increases with $N_{\text{C IV, sys}}$.

3. At each $N_{\text{C IV, sys}}$ bin, the median $N_{\text{H I, sys}}$ and the median $N_{\text{C IV, sys}}$ were selected as independent quantities. This means that there is no C IV system with the chosen median $N_{\text{H I, sys}}$ and $N_{\text{C IV, sys}}$. These median pairs are shown as a function of $N_{\text{H I, sys}}$ in the right panel of Fig. 7.

4. At $\log N_{\text{C IV, sys}} \geq 14.0$, the H I+C IV pairs were binned to $\log N_{\text{H I, sys}} \in [18, 20]$ and $[20, 22]$, as $N_{\text{C IV, sys}}$ is independent of $N_{\text{H I, sys}}$ with a large scatter. For these two $N_{\text{H I, sys}}$ bins, the median $N_{\text{H I, sys}}$ and $N_{\text{C IV, sys}}$ were again selected. These median column density pairs are plotted as the top 2 filled cyan squares in the right panel of Fig. 7.

5. The median $N_{\text{H I, sys}}$ and $N_{\text{C IV, sys}}$ pairs were fitted to Eq. 2, with $C_1 = -1.90 \pm 0.55$, $C_2 = -14.11 \pm 0.19$ and $C_3 = 14.76 \pm 0.17$, respectively. This fit is shown in Fig. 7, along with a 1σ error range.

The fitted curve follows the observed data points much better than a single power-law fit, although the fit might not be the best description due to the lower number of C IV systems at $\log N_{\text{H I, sys}} \in [17, 20]$. Out of our 183 C IV systems, about 75% (137/183) lie in the shaded region. About 16% (30/183) and 9% (16/183) are located outside the 1σ contour at the left side (higher- $N_{\text{C IV, sys}}$) and right side (lower- $N_{\text{C IV, sys}}$) of the fitted curve, respectively. We classify the

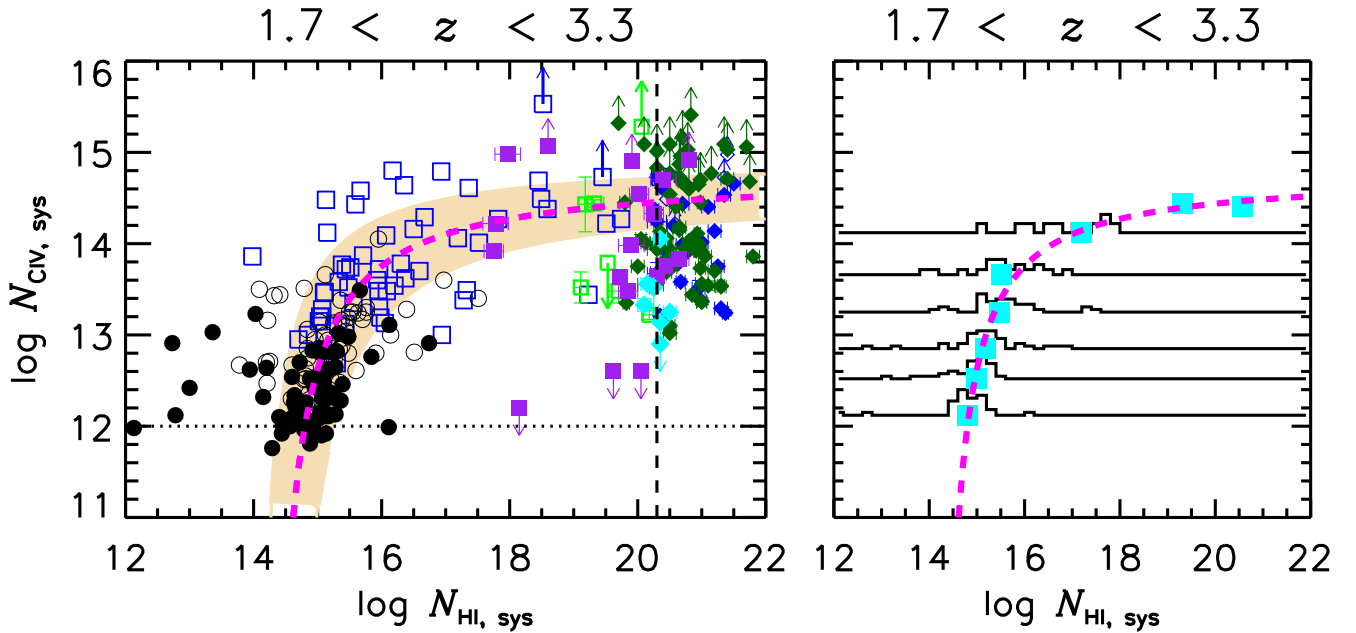


Figure 7. Left panel: The $N_{\text{HI, sys}}-N_{\text{CIV, sys}}$ relation for the $\pm 150 \text{ km s}^{-1}$ range. Filled circles, open circles and blue open squares represent a CIV system having a single-component CIV, a 2-or-3-component CIV and a multi-component CIV. All the other symbols are the same as in Fig. 6. The rectangular hyperbola functional fit to the filled cyan squares in the right panel is shown as the magenta dashed curve with its 1σ range. Right panel: The histogram is the normalised number of CIV systems as a function of $N_{\text{HI, sys}}$, with a binsize of $\Delta \log N_{\text{CIV, sys}} = 0.4$ at $\log N_{\text{CIV, sys}} \in [11.9, 14.3]$. The bottom 6 filled cyan squares overlaid on the histogram indicate the median $N_{\text{HI, sys}}$ and $N_{\text{CIV, sys}}$ in each $N_{\text{HI, sys}}$ bin. The top two squares represent the median $N_{\text{HI, sys}}$ and $N_{\text{CIV, sys}}$ at $\log N_{\text{HI, sys}} \in [18, 20]$ and $[20, 22]$, respectively.

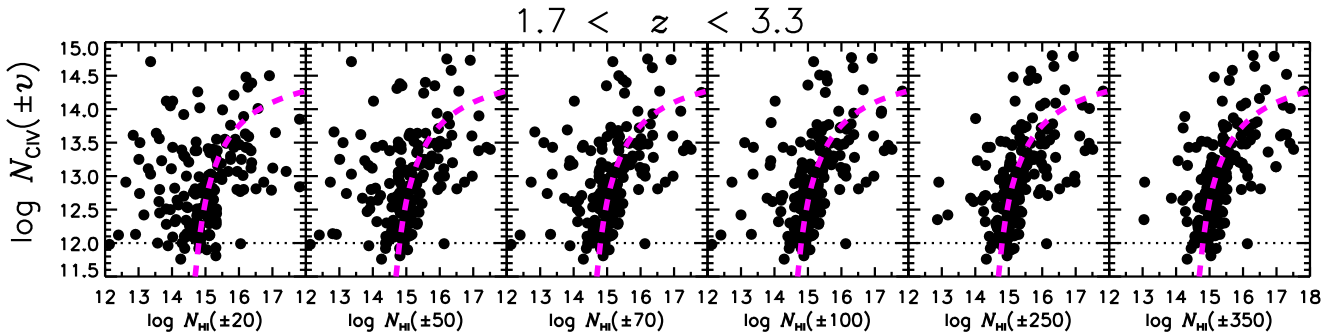


Figure 8. The $N_{\text{HI, sys}}-N_{\text{CIV, sys}}$ relation at 6 different integrated velocity ranges, ± 20 , ± 50 , ± 70 , ± 100 , ± 250 and $\pm 350 \text{ km s}^{-1}$, without extending the velocity range to cover all the continuous CIV absorptions. The y-axis shows the integrated N_{CIV} for the same velocity range as the x-axis, with $v = \pm 20, \pm 50 \text{ km s}^{-1}$, etc. The magenta dashed curve is the rectangular hyperbola fit for the $\pm 150 \text{ km s}^{-1}$ velocity range.

CIV systems into 3 groups, at the left side of, within and at the right side of the 1σ contour as Class “1”, “2” and “3”, respectively. This classification is listed in the 3rd column of Table 2 and is presented in the name of the QSO and the redshift of the CIV system on top of the velocity plot in red for Class “1”, in black for Class “2” and in sky-blue for Class “3”, e.g. Fig. 3.

As $N_{\text{HI, sys}}$ and $N_{\text{CIV, sys}}$ are integrated quantities including many CIV-free HI components, the integrated $N_{\text{HI}}-N_{\text{CIV}}$ relation is likely to depend on the integrated velocity range. Figure 8 shows the $N_{\text{HI, sys}}-N_{\text{CIV, sys}}$ relation at 6 different integrated velocity ranges, ± 20 , ± 50 , ± 70 , ± 100 , ± 250 and $\pm 350 \text{ km s}^{-1}$. Instead of extending the velocity

range to cover all the CIV absorptions of a system, the strict velocity range was used. This results in excluding some CIV components associated with saturated HI components for stronger $N_{\text{CIV, sys}}$ systems, when the integrated velocity range is small. Therefore, a more scatter in the integrated $N_{\text{HI}}-N_{\text{CIV}}$ relation is expected for a smaller integrated velocity range.

The integrated $N_{\text{HI}}-N_{\text{CIV}}$ relation is a scatter relation for the $\pm 20 \text{ km s}^{-1}$ velocity range. Part of this scatter is caused by the way the integrated column densities was calculated. However, part of this scatter is real, implying that there is a small-scale fluctuation in CIV column densities as a function of HI column densities.

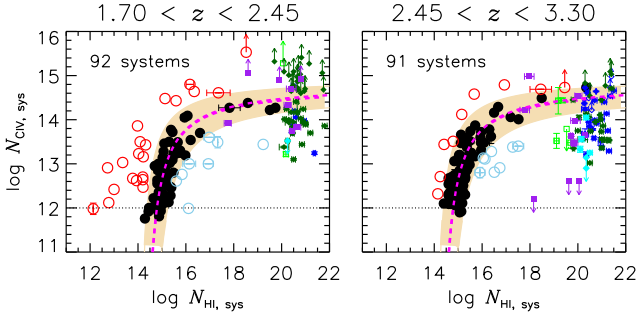


Figure 9. The integrated $N_{\text{H I}}-N_{\text{C IV}}$ relation at the two different redshift bins: $1.70 < z < 2.45$ (left panel) and $2.45 < z < 3.30$ (right panel). The magenta curve represents a simple fitting function to most C IV systems at $1.7 < z < 3.3$ as in Fig. 7. The shaded area indicates the 1σ contour of the fit. Red and sky-blue open circles indicate the C IV systems which are located outside the 1σ contour. All the other symbols are the same as in Fig. 6.

The scatter in the integrated $N_{\text{H I}}-N_{\text{C IV}}$ relation starts to decrease as the integrated velocity range increases. The relation starts to converge at the integrated velocity range larger than $\sim \pm 100 \text{ km s}^{-1}$. There is virtually no difference between the $\pm 250 \text{ km s}^{-1}$ and the $\pm 350 \text{ km s}^{-1}$ velocity range. This is simply due to the fact that higher- $N_{\text{H I}}$ absorbers at $\log N_{\text{H I}, \text{sys}} \geq 14.5$ with which most C IV systems are associated are rare. Another such absorbers can be found at $\gg 1000 \text{ km s}^{-1}$. At the same time, including weak- $N_{\text{H I}}$ absorbers in vicinity of high- $N_{\text{H I}}$ absorbers does not change $N_{\text{H I}, \text{sys}}$ significantly. In short, most C IV systems follow a well-defined integrated $N_{\text{H I}}-N_{\text{C IV}}$ relation at the velocity range larger than $\pm 100 \text{ km s}^{-1}$.

If the rectangular hyperbola function describing most C IV systems is extrapolated at lower- $N_{\text{C IV}, \text{sys}}$, a majority of the Ly α forest with $\log N_{\text{H I}, \text{sys}} < 14$ is expected to be *truly* C IV-free, i.e. $\log N_{\text{C IV}} \ll 11.8$.

5.3 The redshift evolution of the integrated $N_{\text{H I}}-N_{\text{C IV}}$ relation

Figure 9 shows the $N_{\text{H I}, \text{sys}}-N_{\text{C IV}, \text{sys}}$ relation at the two different redshift bins: at $1.70 < z < 2.45$ and at $2.45 < z < 3.30$. The high and low redshift bins were chosen simply to have a similar number of C IV systems in the two bins.

Figure 9 also illustrates two distinct features of the integrated $N_{\text{H I}}-N_{\text{C IV}}$ relation:

1. In the high- z bin, a majority of C IV systems are in the 1σ contour defined at $1.7 < z < 3.3$. Even outliers are very closely located around the 1σ contour. In the low- z bin, normal C IV systems (Class 2, filled circles) are also inside the 1σ contour and have a similar $N_{\text{H I}, \text{sys}}$ spread for a given $N_{\text{C IV}, \text{sys}}$ as in the high- z bin. This implies that most, normal C IV systems do not have any redshift evolution.

2. Higher- $N_{\text{C IV}, \text{sys}}$ systems (Class 1, open red circles) display the most significant difference with redshift. In the low- z bin, they spread into a much lower- $N_{\text{H I}, \text{sys}}$ area in the $N_{\text{H I}, \text{sys}}-N_{\text{C IV}, \text{sys}}$ plane. There are no higher- $N_{\text{C IV}, \text{sys}}$ systems at $\log N_{\text{H I}, \text{sys}} \leq 14$ in the high- z bin. Unfortunately, it is difficult to address the evolution of the lower- $N_{\text{C IV}, \text{sys}}$ systems, since their numbers are too small.

Examination of all higher- $N_{\text{C IV}, \text{sys}}$ systems at low z in

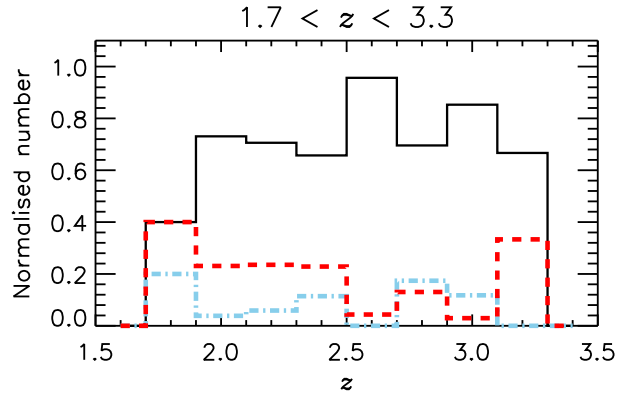


Figure 10. The normalised number of the normal, higher- $N_{\text{C IV}, \text{sys}}$ and lower- $N_{\text{C IV}, \text{sys}}$ C IV systems in black, red dashed and sky-blue dot-dashed histograms at $1.7 < z < 3.3$. The number of C IV systems in each category is normalised by the total number of all C IV systems in the same z bin with the binsize of 0.2. The first ($1.7 < z < 1.9$) and last ($3.1 < z < 3.3$) bins suffer from the low number of C IV systems (5 and 3 systems, respectively), while each of the other z bins samples more than 23 C IV systems.

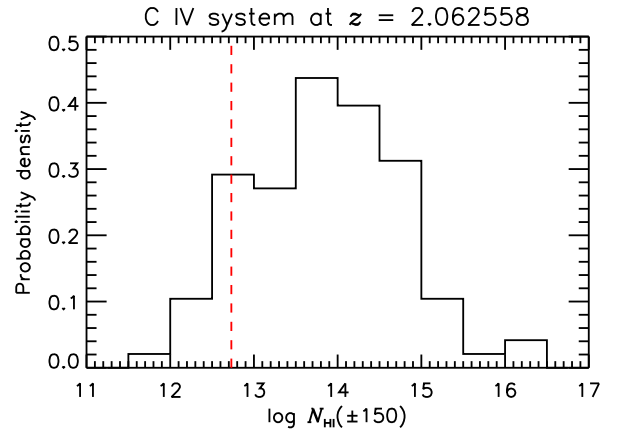


Figure 11. The probability density of an expected $N_{\text{H I}}(\pm 150)$ from 100 realisations, if the higher- $N_{\text{C IV}, \text{sys}}$ C IV system at $z = 2.062558$ toward Q0122-380 is embedded in the forest at $z \sim 2.9$. The vertical dashed line marks the real $\log N_{\text{H I}}(\pm 150) = 12.73$ of the $z = 2.062558$ C IV system.

our sample reveals that about half of them are isolated without any strong H I absorbers within $\pm 200 \text{ km s}^{-1}$, while another half are part of strong, saturated H I absorber complexes. This ratio is also similar at higher z , though in this case there are only 7 higher- $N_{\text{C IV}, \text{sys}}$ systems.

Figure 10 shows the normalised number of 3 categories of C IV systems as a function of z , colour-coded with the symbol colours in Fig. 9. Although the number of our C IV systems is not very large, there seems to be some evidence that the number of higher- $N_{\text{C IV}, \text{sys}}$ systems increases as z decreases.

However, this apparent redshift evolution of higher- $N_{\text{C IV}, \text{sys}}$ systems could be caused by the observational bias, since the H I line number density decreases at lower redshifts (Kim et al. 2013). For an integrated column density over a

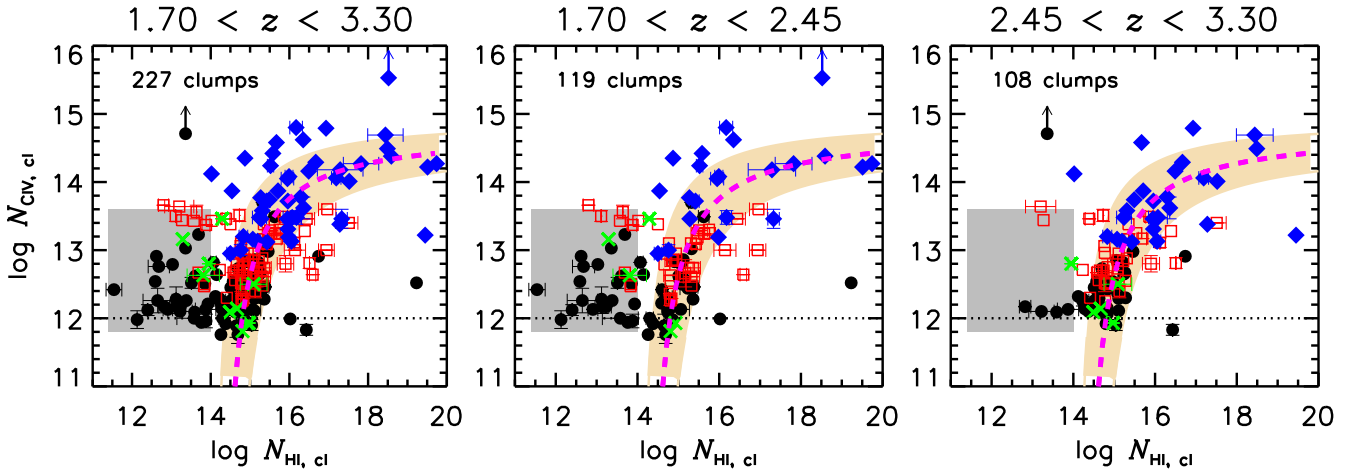


Figure 12. The integrated $N_{\text{HI}}-N_{\text{CIV}}$ relation of C IV clumps at the 2 different redshift bins with the left panel for the full redshift range. Filled circles and open red squares represent a clump with a single C IV component and 2-or-3 C IV components, respectively. Filled blue diamonds represent a clump with more than 4 C IV components, while green crosses indicate a uncertain clump. All the rest of the symbols are the same as in Fig. 9, including the magenta rectangular hyperbola curve. The grey-shaded area is where most higher- N_{CIV} clumps are located. For clarity, the coloured version is available online.

fixed velocity range, stronger blending at higher z would result in including more C IV-free H I components.

To illustrate this point, Fig. 11 shows the probability density of an expected $N_{\text{HI}}(\pm 150)$, if the higher- $N_{\text{CIV, sys}}$ C IV system at $z = 2.062558$ toward Q0122-380 is embedded in the forest at $z \sim 2.9$. We used part of the real spectrum at $z \sim 2.9$ of PKS2126-158, Q0420-388, Q0636+6801 and HE0940-1050. This C IV absorption feature is initially placed at 6007 \AA ($z = 2.880$) in one of the 4 spectra. An integrated $N_{\text{HI}}(\pm 150)$ was calculated for this redshift. Then, the C IV component was shifted by 4 \AA up to 6103 \AA ($z = 2.942$). For each shift, a new integrated $N_{\text{HI}}(\pm 150)$ was calculated. This process was repeated for the remaining 3 QSO spectra, with a total of 100 realisations.

Considering that the $z = 2.062558$ C IV system has the real $N_{\text{HI}}(\pm 150) = 12.73 \pm 0.04$, the probability density peaks at $N_{\text{HI}}(\pm 150) \sim 14$. In short, higher- $N_{\text{CIV, sys}}$ systems at $z \sim 2$ could be a normal C IV systems at $z \sim 2.9$, perfectly within the 1σ range in Fig. 7 for its $N_{\text{CIV}}(\pm 150) = 12.91 \pm 0.01$.

However, this simple deduction has a one significant flaw. In the above 100 realisations, both H I and C IV were treated as being independent, which is not correct. If higher- $N_{\text{CIV, sys}}$ systems started to pop up mainly due to the lower H I line number density at lower redshifts, the same logic should apply for normal C IV systems. This would shift the fitted dashed curve in the low- z bin to the left side in Fig. 9, while no such evolution is observed. Therefore, the increasing number of higher- $N_{\text{CIV, sys}}$ systems at lower redshifts is likely to be real, not a consequence of less blending.

5.4 The integrated $N_{\text{HI}}-N_{\text{CIV}}$ relation of C IV clumps

Our definition of a C IV system includes many nearby C IV-free H I absorptions. Therefore, a term “clump” was introduced in Section 4.3, in order to assign C IV only with the clearly associated H I in the velocity space. First, a C IV clump velocity range is defined for which a C IV profile wing

recovers to a normalised C IV flux $F_{\text{CIV}} = 1$ longer than 5 km s^{-1} . Then, only the H I components in the clump velocity range are associated with the C IV clump, e.g. Figs. 3 and 4. Depending on the H I and C IV profiles, a system can consist of a single clump or many clumps.

As defining a clump can be subjective, due to the uncertainties in the continuum and non-unique H I component structures from the Voigt profile fitting, an auxiliary term “Ly $\alpha\beta$ clump” was also introduced. For this definition, 1) a velocity range is chosen for a C IV absorption profile wing to recover to $F_{\text{CIV}} \geq 0.98$ and 2) H I absorption profiles from Ly α and Ly β are also clearly separable at similar relative velocities as C IV. This definition is based largely on the profile shape. The Ly $\alpha\beta$ clump is closest to a conventionally defined C IV absorber/system in literature.

Figures 12 and 13 show the integrated $N_{\text{HI}}-N_{\text{CIV}}$ relation for clumps and Ly $\alpha\beta$ clumps, respectively. The $N_{\text{HI, cl}}-N_{\text{CIV, cl}}$ relation of clumps displays much more scatter than the C IV systems, which is rather similar to the $N_{\text{HI, sys}}-N_{\text{CIV, sys}}$ relation with an integrated velocity range less than $\pm 50 \text{ km s}^{-1}$, as seen in Fig. 8. This is expected since $N_{\text{HI, cl}}$ and $N_{\text{CIV, cl}}$ of most clumps are measured at a smaller velocity range than $\pm 150 \text{ km s}^{-1}$.

The scatter is mainly spread into a gray-shaded area in the left side of the hyperbolic fit curve in the low- z bin, where most higher- N_{CIV} systems are located. In contrast, in the high- z bin, clumps are distributed mostly along the hyperbolic fit curve. Similar to C IV systems, higher- N_{CIV} clumps are mostly found at lower redshifts.

Qualitatively, Ly $\alpha\beta$ clumps also show a similar trend on the $N_{\text{HI, } \alpha\beta \text{ clump}}-N_{\text{CIV, } \alpha\beta \text{ clump}}$ plane. This is mainly caused by the fact that most H I components just outside the clump velocity bound are usually weak. In addition, clumps/Ly $\alpha\beta$ clumps in the gray-shaded area have only one C IV component and $\log N_{\text{HI, cl}} \leq 14$, i.e. unsaturated, which enables to obtain a reliable H I component structure from a Ly α only. Therefore, an integrated velocity range for clumps and Ly $\alpha\beta$ clumps in the gray-shaded area is the same in most cases.

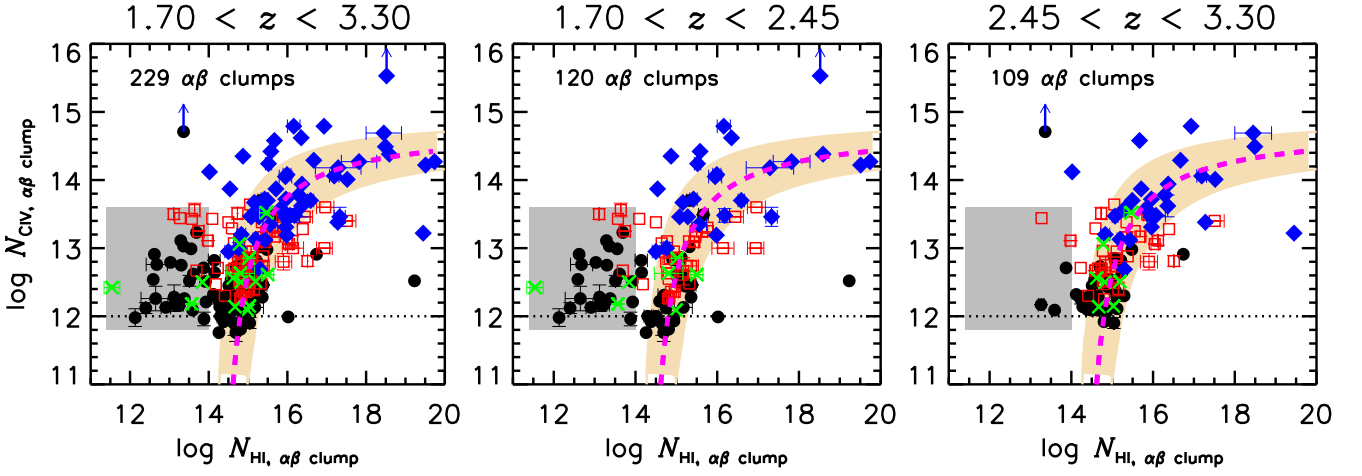


Figure 13. The integrated $N_{\text{HI}}-N_{\text{CIV}}$ relation of C IV Ly $\alpha\beta$ clumps at the 2 different redshift bins with the left panel for the full redshift range. All the symbols are the same as in Fig. 12. The online, coloured version is available for a clear view.

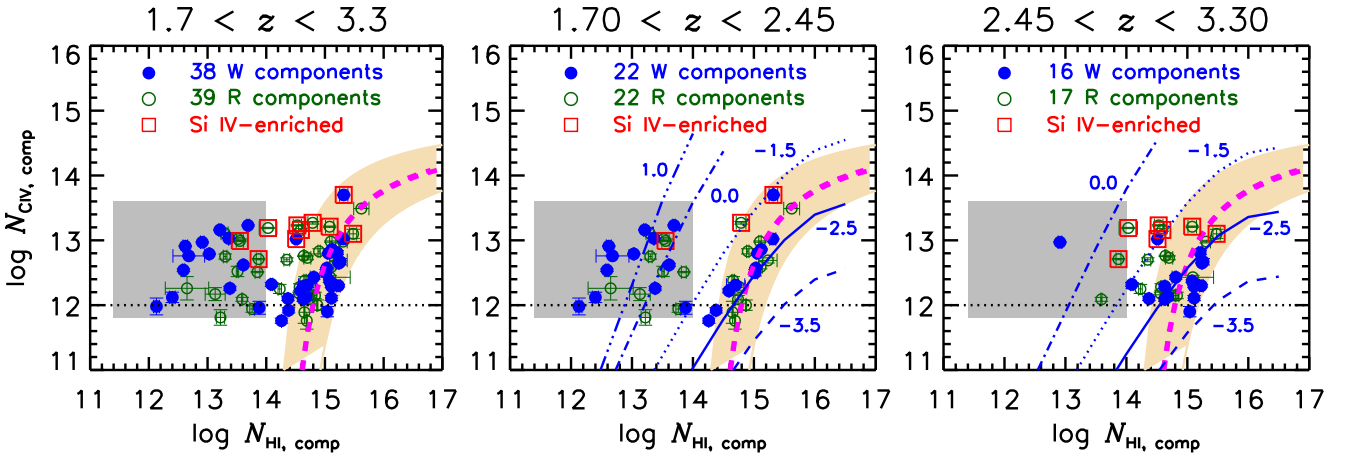


Figure 14. The component $N_{\text{HI}}-N_{\text{CIV}}$ relation at the 2 different redshift bins with the left panel for the full redshift range. Filled and open circles represent the 38 well-aligned (W) and 39 reasonably-aligned (R) H I+C IV component pairs, respectively. The symbols in larger red open squares indicate the aligned pairs with an aligned Si IV component. The magenta curve is the same as in Fig. 7. The gray-shaded area delineates the same gray-shaded region in Fig. 13, and is the region populated mainly by higher- N_{CIV} systems and clumps. The blue dashed, solid, dotted, dot-dashed and dot-dot-dot-dashed curves represent the CLOUDY predictions with the fiducial Schaye $n_{\text{H}}-N_{\text{HI}}$ relation for $[\text{C}/\text{H}] = -3.5, -2.5, -1.5, 0.0$ and 1.0 , respectively, noted with a number next to the corresponding curve.

6 C IV COMPONENTS

6.1 Photoionisation modelling

The integrated relations presented in Section 5 hold for averaged quantities, without considering actual one-to-one physical association between H I and C IV. Therefore, any attempt to derive physical conditions of the absorbing gas based on the integrated $N_{\text{HI}}-N_{\text{CIV}}$ relation, such as the carbon abundance, is meaningless. However, for aligned components with the difference between the velocity centroid of relatively clean H I and C IV components less than 5 km s^{-1} , which can be assumed to be co-spatial, an analysis based on photoionisation equilibrium becomes possible. We note that only 12% of the total of 628 C IV components are aligned, as expected from strong evidence of a velocity difference between H I and C IV (Ellison et al. 2000; Reimers et al. 2001).

Therefore, the aligned pairs do not represent a majority of H I and C IV absorbing gas, but only sample the gas having a simple physical structure. We also note that only 13% (10 out of 77 pairs) aligned pairs have an aligned Si IV component.

The internal thermal and chemical structures of optically-thin H I absorbers with $\log N_{\text{HI, comp}} < 17.2$ such as our aligned H I components are mainly determined by photoionisation and photoheating from the ambient ultraviolet (UV) background radiation balanced by adiabatic cooling in the expanding Universe, i.e. the Hubble expansion, and by radiative cooling (Hui & Gnedin 1997; Schaye et al. 2000; Schaye 2001; Wiersma et al. 2009; Davé et al. 2010). At $z \sim 2.4$, the cosmic mean density corresponds to the total (neutral and ionised) hydrogen volume density $\log n_{\text{H}} \sim -6.72 + 3 \times \log(1+z) \sim -5.13 [\text{cm}^{-3}]$ (Wiersma et al. 2009).

Any absorbers below this density need to be taken account of the Hubble expansion, while absorbers above this density expect to collapse. Based on the subset of our well-aligned H I+C IV component pairs, Kim et al. (2016) find that most H I components aligned with C IV and C III at $\log N_{\text{H I, comp}} \leq 16$ have $\log n_{\text{H}} \in [-5.2, -3.3]$ at $z \sim 2.4$. Since n_{H} of our H I+C IV pairs is close to the cosmic mean density, we assume that both Hubble expansion and gravitational collapse do not play a significant role, i.e. a static absorber. This assumption leaves radiative cooling the dominant source of cooling of these optically-thin absorbers. In addition, Kim et al. (2016) also find that most aligned, optically-thin H I+C IV absorbers have the gas temperature in K at $\log T \in [3.5, 5.5]$ peaking at $\log T \sim 4.4 \pm 0.3$, implying that the photoionisation model can be considered to be adequate for our aligned H I+C IV component pairs in this study.

To model the gas clouds, we used the photoionisation code CLOUDY version c10.3 (Ferland et al. 2013). The geometry of the gas was assumed as a uniform slab in thermal and ionisation equilibrium, and we used the redshift-dependent CLOUDY-default UV background, the Haardt-Madau (HM) UVB 2005 version with contributions from both QSOs and galaxies (Q+G). For the two redshift ranges at $1.70 < z < 2.45$ and $2.45 < z < 3.30$, we used the HM Q+G UVB 2005 at $z = 2.3$ and $z = 2.8$ since a large fraction of the pairs has a redshift similar to the adopted one. The CLOUDY-default solar abundance pattern was used, with the solar carbon abundance of $(\text{C}/\text{H})_{\odot} = -3.61$. The carbon abundance is expressed in the usual way as $[\text{C}/\text{H}] = \log(\text{C}/\text{H}) - \log(\text{C}/\text{H})_{\odot}$.

For an assumed UV background, deriving physical parameters of H I+C IV gas requires an additional carbon transition such as C II or C III to break a degeneracy between unknown $[\text{C}/\text{H}]$ and $\log n_{\text{H}}$. Since estimating a reliable $N_{\text{C III}}$ or $N_{\text{C II}}$ is not possible for a majority of our H I+C IV pairs due to blending, we instead generated a set of grid models with $[\text{C}/\text{H}]$ varying from -3.5 to 2.0 with the logarithmic step size of 0.5 , with $\log n_{\text{H}}$ from -7.0 to 0.0 with the logarithmic step size of 0.2 , and with $\log N_{\text{H I}}$ as a stopping criterion varying from 12 to 16.5 with the logarithmic step size of 0.5 . Then, to break a degeneracy, we used the $n_{\text{H}}-N_{\text{H I}}$ relation by Schaye (2001) as our fiducial Schaye relation, $\log N_{\text{H I}} \sim 20.86 + 1.5 \log n_{\text{H}}$, for the low-density forest in hydrostatic equilibrium, using his default values for the gas temperature, the UVB and the gas mass fraction.

6.2 The $N_{\text{H I}}-N_{\text{C IV}}$ relation of C IV components

Figure 14 shows the component $N_{\text{H I}}-N_{\text{C IV}}$ ($N_{\text{H I, comp}}-N_{\text{C IV, comp}}$) relation. As with the $N_{\text{H I, cl}}-N_{\text{C IV, cl}}$ relation shown in Fig. 12, the H I+C IV component pairs also display a scatter plot. The pairs with an aligned Si IV tend to have higher $N_{\text{C IV, comp}}$ and appear predominantly at higher redshifts.

The pairs occupy a well-defined region on the $N_{\text{H I, comp}}-N_{\text{C IV, comp}}$ plane at $(\log N_{\text{H I, comp}}, \log N_{\text{C IV, comp}}) = (12.0-15.5, 11.7-13.5)$, without any pairs with strong H I and C IV. This is largely due to the fact that

(i) strong H I and C IV absorptions break into several weaker components,

(ii) a majority of the C IV components are not at the same velocity as H I (Ellison et al. 2000; Reimers et al. 2001), and

(iii) the velocity structure of the strong H I gas is less well resolved than the strong C IV gas due to the larger H I thermal broadening.

In Fig. 14, we also show the CLOUDY predictions, with $[\text{C}/\text{H}]$ noted next to each curve. At $z \sim 2.1$, the aligned pairs are clustered as the two distinct groups. The pairs around the hyperbolic fit seem to be well-modeled with $[\text{C}/\text{H}] \sim -2.5$ and the fiducial Schaye $n_{\text{H}}-N_{\text{H I}}$ relation. Other $[\text{C}/\text{H}]$ values do not predict the observed $N_{\text{H I, comp}}-N_{\text{C IV, comp}}$ relation as well as $[\text{C}/\text{H}] = -2.5$, regardless of any assumed $n_{\text{H}}-N_{\text{H I}}$ relations other than the Schaye $n_{\text{H}}-N_{\text{H I}}$ relation. On the other hand, the pairs inside the gray-shaded area on the $N_{\text{H I, comp}}-N_{\text{C IV, comp}}$ plane can be produced only with $[\text{C}/\text{H}] \geq 0.0$ at $\log n_{\text{H}} \in [-6.0, -5.0]$ (Schaye et al. 2007), reinforcing that they are likely to be connected with star formations at $z \sim 2.1$.

At $z \sim 2.9$, the aligned pairs are predominantly in one region. The Schaye $n_{\text{H}}-N_{\text{H I}}$ relation at $[\text{C}/\text{H}] = -2.5$ is less satisfactory than at lower redshifts, implying that the high- z aligned pairs sample a wider range of physical conditions than those around the rectangular hyperbola curve at $z \sim 2.1$. For the same $[\text{C}/\text{H}]$, Si IV-enriched H I+C IV pairs have a higher physical density than Si IV-free pairs, as the Schaye relation assumes a higher n_{H} for higher $N_{\text{H I}}$. For a similar n_{H} , i.e. a similar $N_{\text{H I}}$, Si IV-enriched pairs have a higher $[\text{C}/\text{H}]$ than Si IV-free pairs.

On face value, without taking account of any possible selection bias, our aligned H I+C IV pairs seem to evolve to have lower $N_{\text{H I}}$ at lower z , if aligned pairs are produced by the gas in a similar location, i.e. an IGM filament gas or a galactic halo, suggested by their low physical gas density.

6.3 $N_{\text{C IV, comp}}/N_{\text{H I, comp}}$ as a function of $N_{\text{H I, comp}}$

The ratio $N_{\text{C IV, comp}}$ over $N_{\text{H I, comp}}$ provides, after ionisation corrections (which may be large), a measure of $[\text{C}/\text{H}]$. Not surprisingly, given that $N_{\text{C IV, comp}}$ is largely independent of $N_{\text{H I, comp}}$ (see Fig. 14), this ratio is very closely inversely proportional to $N_{\text{H I, comp}}$ as can be seen in Fig. 15. A formal fit over the full redshift range gives $\log(N_{\text{C IV, comp}}/N_{\text{H I, comp}}) = (12.07 \pm 0.83) + (-0.97 \pm 0.06) \times \log N_{\text{H I, comp}}$, or, expressed slightly differently, $\log N_{\text{C IV, comp}} = (12.07 \pm 0.83) + (0.03 \pm 0.06) \times \log N_{\text{H I, comp}}$.

Over the column density range $\log N_{\text{H I, comp}} \in [14, 16]$ for the full redshift range, the median $\log(N_{\text{C IV, comp}}/N_{\text{H I, comp}}) = -2.38$ for the median $\log N_{\text{H I, comp}} = 14.8$. This is close to the value -2.46 found by Cowie et al. (1995) for a similar $N_{\text{H I}}$ range at $z \sim 2.6$. For the column density range $\log N_{\text{H I, comp}} \in [12, 14]$, the median $\log(N_{\text{C IV, comp}}/N_{\text{H I, comp}}) = -0.50$ and the median $\log N_{\text{H I, comp}} = 13.3$.

The aligned pairs with highest $N_{\text{C IV, comp}}/N_{\text{H I, comp}}$ for a given $N_{\text{H I, comp}}$ are Si IV-enriched components (symbols embedded in a larger open red square). This suggests that the aligned pairs with Si IV have a higher total hydrogen volume density and/or a higher metallicity than Si IV-free pairs as seen in Fig. 14.

Assuming that the intensity and spectral shape of the UV ionising background do not change significantly at

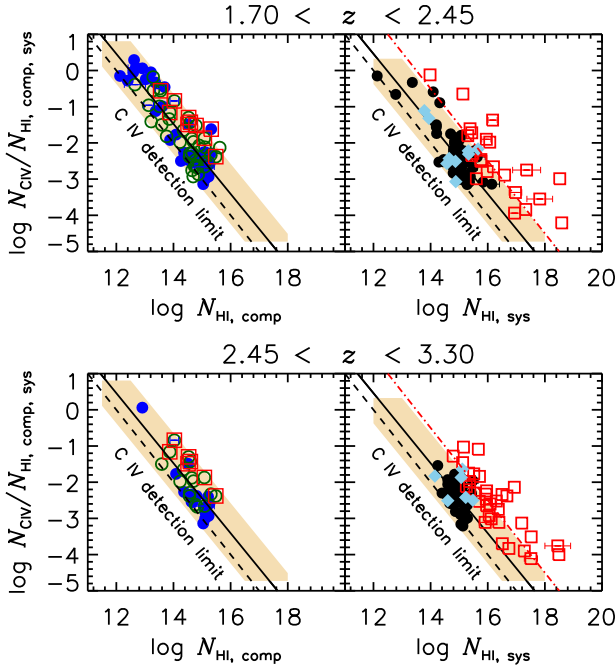


Figure 15. *Left panels:* The $N_{\text{H I, comp}}-(N_{\text{C IV, comp}}/N_{\text{H I, comp}})$ relation at $1.70 < z < 2.45$ (upper panel) and $2.45 < z < 3.30$ (lower panel). The symbols are the same as in Fig. 14. *Right panels:* The $N_{\text{H I, sys}}-(N_{\text{C IV, sys}}/N_{\text{H I, sys}})$ relation for the C IV systems. Filled circles, filled sky-blue diamonds and open red squares indicate Si IV-free, blended/uncertain-Si IV and Si IV-enriched C IV systems. In all panels, the solid line represents a least-square-fit to the $N_{\text{C IV, comp}}/N_{\text{H I, comp}}$ at the full redshift range: $\log(N_{\text{C IV, comp}}/N_{\text{H I, comp}}) = (12.07 \pm 0.83) + (-0.97 \pm 0.06) \times \log N_{\text{H I, comp}}$. The light-orange shaded area represents the 1σ contour. The black dashed line delineates a typical C IV detection limit of $\log N_{\text{C IV, comp}} = 12.0$. The overlaid red dot-dashed line in the right panels is the best-fit to the Si IV-enriched C IV systems: $\log(N_{\text{C IV, sys}}/N_{\text{H I, sys}}) = 13.5 - \log N_{\text{H I, sys}}$. Only errors larger than the symbol size are displayed.

$2 < z < 3.3$ (Bolton et al. 2005; Faucher-Giguère et al. 2008; Boksenberg & Sargent 2015) and that additional photons from other ionising sources are negligible for aligned C IV components at our $N_{\text{H I, comp}}$ range, a higher $N_{\text{C IV, comp}}/N_{\text{H I, comp}}$ at lower- $N_{\text{H I, comp}}$ implies a higher carbon abundance in lower- $N_{\text{H I, comp}}$ pairs or a higher gas volume density if a similar carbon abundance, e.g. Schaye et al. (2007).

The interpretation of $N_{\text{C IV, sys}}/N_{\text{H I, sys}}$ for C IV systems shown in Fig. 15 is less straightforward since they are averaged quantities. Comparing Figs. 8 and 9 with Fig. 14 shows that C IV systems display a larger scatter in $N_{\text{C IV, sys}}$ for a given $N_{\text{H I, sys}}$ than the components. Therefore, the C IV systems display a larger scatter in the $N_{\text{H I, sys}}-(N_{\text{C IV, sys}}/N_{\text{H I, sys}})$ relation. Si IV-free $N_{\text{C IV, sys}}$ and blended/uncertain-Si IV $N_{\text{C IV, sys}}$ systems follow the $N_{\text{H I, comp}}-(N_{\text{C IV, comp}}/N_{\text{H I, comp}})$ relation reasonably well, with the median $\log(N_{\text{C IV, sys}}/N_{\text{H I, sys}}) = -2.40$ for the full redshift and $N_{\text{H I, sys}}$ ranges.

On the other hand, the Si IV-enriched C IV systems (open red squares) show an order of magnitude higher $N_{\text{C IV, sys}}/N_{\text{H I, sys}}$ for a given $N_{\text{H I, sys}}$. This indicates that Si IV-enriched C IV systems are exposed to a higher UV back-

ground if the gas density and metallicity are similar to the Si IV-free systems at a similar $N_{\text{H I, sys}}$, or alternatively have a higher $[\text{C}/\text{H}]$ and n_{H} for the same UVB.

6.4 CLOUDY predictions for $N_{\text{C IV, comp}}/N_{\text{H I, comp}}$ as a function of $N_{\text{H I, comp}}$

Figure 16 shows the observed $N_{\text{H I, comp}}-(N_{\text{C IV, comp}}/N_{\text{H I, comp}})$ plane overlaid with the CLOUDY predictions at $2.45 < z < 3.30$ and at $1.70 < z < 2.45$ for four different carbon abundances.

For $2.45 < z < 3.30$:

(i) The aligned pairs have $[\text{C}/\text{H}] \geq -3.5$. This $[\text{C}/\text{H}] \sim -3.5$ is the estimated median IGM metallicity from a pixel optical depth analysis by Schaye et al. (2003). That study uses all the H I absorption components including those without actual C IV detections above a detection limit. At $z \sim 2.5$, the fraction of C IV-enriched absorbers at $\log N_{\text{H I}} \sim 15$ is about 50%. This fraction decreases rapidly as $\log N_{\text{H I}}$ decreases, while the number of absorbers at $\log N_{\text{H I}} \in [13, 15]$ is about 19 times larger than the ones at $\log N_{\text{H I}} \geq 15$ (Kim et al. 2013). Therefore, our $[\text{C}/\text{H}]$ limit on the aligned pairs with detected C IV absorption should be higher. In general, $[\text{C}/\text{H}]$ spans at $[-3.5, -1.0]$ if $\log n_{\text{H}} \sim -3.8$, i.e. the total hydrogen volume density which produces the maximal $N_{\text{C IV, comp}}/N_{\text{H I, comp}}$ at $[\text{C}/\text{H}] \in [-3.5, -1.0]$. However, if we choose $[\text{C}/\text{H}] \sim -1.0$, $\log n_{\text{H}}$ of most aligned pairs ranges from -3.2 to -2.3 .

(ii) At $[\text{C}/\text{H}] = -2.5$, the median $N_{\text{C IV, comp}}/N_{\text{H I, comp}}$ of the well-aligned pairs (filled blue circles) can be reproduced approximately by the Schaye $n_{\text{H}}-N_{\text{H I}}$ relation, with a scatter both in $[\text{C}/\text{H}]$ and n_{H} . We can obtain a good empirical fit for the well-aligned pairs with the $n_{\text{H}}-N_{\text{H I}}$ relation, $\log n_{\text{H}} = -18.4 + \log N_{\text{H I}}$, while the reasonably-aligned pairs clearly have a higher $[\text{C}/\text{H}]$. We note that this empirical fit does not have any physical basis, but only depends on the observed data and that the empirical best-fit $n_{\text{H}}-N_{\text{H I}}$ relation differs for a different $[\text{C}/\text{H}]$.

(iii) An empirical best-fit $n_{\text{H}}-N_{\text{H I}}$ relation with $[\text{C}/\text{H}] = -1.0$, $\log n_{\text{H}} = -10.6 + 0.55 \times \log N_{\text{H I}}$, provides an overall good fit to all the aligned pairs.

For $1.70 < z < 2.45$:

(i) For the data points at $(N_{\text{C IV, comp}}/N_{\text{H I, comp}}) \sim -2.4$, the Schaye $n_{\text{H}}-N_{\text{H I}}$ relation with $[\text{C}/\text{H}] = -2.5$ reproduces the observations reasonably well, with a small scatter in $\Delta[\text{C}/\text{H}] \sim \pm 0.5$.

(ii) On the other hand, the data points at $\log(N_{\text{C IV, comp}}/N_{\text{H I, comp}}) \geq -1.5$ and $\log N_{\text{H I, comp}} \leq 14$ require $[\text{C}/\text{H}] \geq -1.0$. If $\log n_{\text{H}} \sim -3.8$, their $[\text{C}/\text{H}]$ spans from -1.0 to 0.0 . With the Schaye $n_{\text{H}}-N_{\text{H I}}$ relation, $[\text{C}/\text{H}]$ has to be $0.0 \sim 2.0$.

(iii) The two distinct groups in terms of $N_{\text{C IV, comp}}/N_{\text{H I, comp}}$ and the $N_{\text{H I, comp}}-N_{\text{C IV, comp}}$ relation at $z \sim 2.1$ probably arise from different physical conditions.

(iv) The aligned pairs grouped around at $\log(N_{\text{C IV, comp}}/N_{\text{H I, comp}}) \sim -2.4$ do not seem to show a noticeable redshift-dependence on $[\text{C}/\text{H}]$.

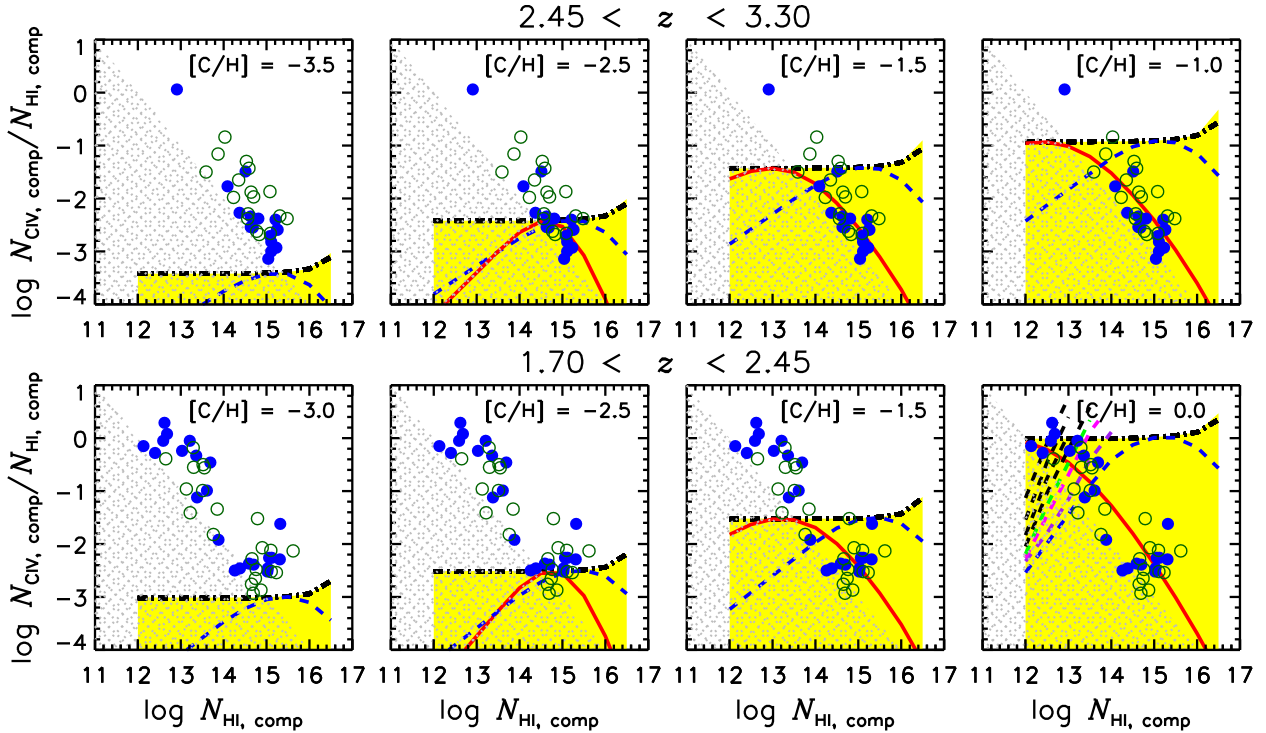


Figure 16. Upper (lower) panels show the $N_{\text{HI, comp}}-(N_{\text{CIV, comp}}/N_{\text{HI, comp}})$ relation at $2.45 < z < 3.30$ ($1.70 < z < 2.45$) at four $[\text{C}/\text{H}]$ noted in each panel. The symbols are the observed data points as in the left panels of Fig. 14. The gray-shaded area represents the region where the current observations cannot reach due to detection limit. The yellow-shaded region covers the $N_{\text{HI, comp}}-(N_{\text{CIV, comp}}/N_{\text{HI, comp}})$ parameter space predicted by CLOUDY with the total hydrogen volume density $\log n_{\text{H}} \in [-5, 0]$. The dot-dashed curve at the upper boundary of the yellow-shaded region delineates $\log n_{\text{H}} = -3.8$, around which the highest possible $N_{\text{CIV, comp}}/N_{\text{HI, comp}}$ is predicted for a given $[\text{C}/\text{H}]$. Overlaid curves are the CLOUDY-predicted $N_{\text{HI, comp}}-(N_{\text{CIV, comp}}/N_{\text{HI, comp}})$ relation with a different $n_{\text{H}}-N_{\text{HI}}$ relation. The blue dashed curve is for the fiducial Schaye $n_{\text{H}}-N_{\text{HI}}$ relation. The red solid curve is the predicted $N_{\text{HI, comp}}-(N_{\text{CIV, comp}}/N_{\text{HI, comp}})$ relation for the best-fit empirical $n_{\text{H}}-N_{\text{HI}}$ relation, $\log n_{\text{H}} = A + B \times \log N_{\text{HI}}$. At $2.45 < z < 3.30$, $(A, B) = (-18.4, 1.0)$, $(-11.6, 0.6)$ and $(-10.6, 0.55)$ for $[\text{C}/\text{H}] = -2.5, -1.5$ and -1.0 , respectively. At $1.70 < z < 2.45$, $(A, B) = (-18.4, 1.0)$, $(-11.6, 0.6)$ and $(-9.5, 0.5)$ for $[\text{C}/\text{H}] = -2.5, -1.5$ and 0.0 , respectively. In the lower right panel, several dashed curves above the blue dashed curve indicates the CLOUDY predictions for the Schaye $n_{\text{H}}-N_{\text{HI}}$ relation at $[\text{C}/\text{H}] = 0.5, 1.0, 1.2, 1.4, 1.6, 1.8$ and 2.0 , respectively.

6.5 The velocity offset between H I and C IV components

One of the predictions from the $N_{\text{HI, sys}}-N_{\text{CIV, sys}}$ relation, if we extrapolate, is that the majority of the Ly α forest at $\log N_{\text{HI, comp}} < 14$ might be *truly* C IV-free, i.e. $\log N_{\text{CIV, comp}} \ll 11.8$, especially at high redshifts. This is in good agreement with the finding from the stacking analysis by Ellison et al. (2000). They de-redshifted the absorption-free C IV regions associated with 67 H I components at $\log N_{\text{HI, comp}} \in [13.5, 14.0]$ at $z \sim 3.45$ from 2 Keck/HIRES spectra. All the de-redshifted C IV regions were then co-added to produce a $S/N = 1250$ stacked spectrum. No absorption was seen at down to $\log N_{\text{CIV, comp}} \sim 10.6$ (converted from the quoted C IV detection limit of 0.15 mÅ at 4σ).

However, this result from the stacking analysis is valid only when the absorption centroids of H I and C IV occur at the same relative velocity (Lu & Savage 1993; Ellison et al. 2000; Pieri et al. 2010). When the velocity offset is random, then adopting the H I redshift will result in a smearing out any weak C IV absorptions. Indeed, Ellison et al. (2000) have found a velocity offset between H I and C IV at $\log N_{\text{HI}} \in [13.6, 16.0]$ with a dispersion of $\sim 17 \text{ km s}^{-1}$ at $z \sim 3.45$. A

similar velocity offset was also found between H I and O VI, and O VI and C IV at $z \sim 1.5$ (Reimers et al. 2001).

As our N_{HI} was measured using higher Lyman orders, thus revealing a more reliable H I component structure, we checked the velocity offset between H I and C IV centroids. These are shown in Fig. 17. Among 97 single-C IV-component clumps including *uncertain* clumps (the 6th column of Table 3), we selected 95 clumps with unsaturated C IV and $\log N_{\text{HI, cl}} \leq 17$, since the stacking analysis is primarily applied for low- N_{HI} H I components with no C IV and since only the strongest C IV component would appear due to noise. Out of 95, 30 clumps are associated with unsaturated H I Ly α (Sample I, blue filled circles) and 65 clumps have saturated Ly α (Sample II, gray open circles). Note that most Sample I clumps are higher- $N_{\text{CIV, sys}}$ systems.

In both upper panels of Fig. 17, the velocity offset Δv_{small} is calculated between the C IV flux minimum and the closest H I component. A velocity offset is clearly present, but without any trend with $N_{\text{CIV, comp}}$, nor with $N_{\text{HI, comp}}$. C IV components with a large velocity offset are the ones whose C IV flux minimum is at the wing of H I profiles, such as the $z = 2.521424$ clump toward Q0002-422. For 30 C IV components of Sample I, the mean and median velocity offsets are $0.7 \pm 7.0 \text{ km s}^{-1}$ and 0.2 km s^{-1} , respectively. For

the remaining 65 clumps of Sample II, the mean and median velocity offset is $-2.5 \pm 12.8 \text{ km s}^{-1}$ and -1.5 km s^{-1} . For the full 95 components, the mean and median velocity offsets are $-1.5 \pm 11.3 \text{ km s}^{-1}$ and -0.6 km s^{-1} . There is no clear redshift dependence on Δv_{small} .

The velocity offset Δv_{strong} is between the C IV flux minimum and the strongest H I components in the selected clumps. For Sample I (Sample II), the mean and median velocity offset is $-0.1 \pm 7.0 \text{ km s}^{-1}$ ($-2.6 \pm 13.1 \text{ km s}^{-1}$) and -0.2 km s^{-1} (-1.4 km s^{-1}). There is no noticeable difference between Δv_{small} and Δv_{strong} , as seen in the lower panel of Fig. 17. For the full 95 components, the mean and median Δv_{strong} is $-1.8 \pm 11.6 \text{ km s}^{-1}$ and -0.6 km s^{-1} .

Our standard deviation of Δv_{small} and Δv_{strong} for the full sample is about a factor of 1.5 smaller than the one found by Ellison et al. (2000). About 58% (55 out of 95 clumps) have Δv_{small} less than 5 km s^{-1} . The minimum b value of C IV in the single-C IV-component clumps is 4.7 km s^{-1} with a median b of 11.5 km s^{-1} and a 1σ of 6.0 km s^{-1} . Therefore, the stacking analysis could decrease the absorption flux by a factor of about two. This implies that $\log(N_{\text{C IV, comp}}/N_{\text{H I, comp}})$ could decrease by about 0.3 dex than its true value by stacking, or increase its detection limit by the same amount. However, considering a large observational scatter seen in $\log(N_{\text{C IV, comp}}/N_{\text{H I, comp}})$ vs $\log N_{\text{H I, comp}}$ (see Fig. 16), a possible [C/H] range derived from CLOUDY modelings on the stacked data is not affected significantly.

7 THE ORIGIN OF THE INTEGRATED $N_{\text{H I}}-N_{\text{C IV}}$ RELATION FOR C IV SYSTEMS

7.1 Dependence of the $N_{\text{H I, sys}}-N_{\text{C IV, sys}}$ relation on other ions

Figure 18 shows the integrated $N_{\text{H I}}-N_{\text{C IV}}$ relation of C IV systems, separated into groups set by the existence or otherwise of Si IV, O VI and N V. Any systems with blended, uncertain or not covered Si IV are excluded. The left and middle panels show the $N_{\text{H I, sys}}-N_{\text{C IV, sys}}$ relation of Si IV-enriched and Si IV-free C IV systems, regardless of existence of O VI and N V. Si IV-enriched C IV systems show a scatter around the hyperbola fit curve, even though they occupy in a reasonably well-defined area at $(\log N_{\text{H I, sys}}, \log N_{\text{C IV, sys}}) = (14.0-19.0, 12.8-15.0)$. However, 84% of Si IV-free C IV systems (87 out of 103 systems) lie close to the curve at the lower- $N_{\text{C IV, sys}}$ end, with a few higher- $N_{\text{C IV, sys}}$ systems.

Figure 18 also shows that the $N_{\text{H I, sys}}-N_{\text{C IV, sys}}$ relation for systems with O VI and/or N V. Due to the difficulty in detecting the O VI $\lambda\lambda 1031, 1037$ doublet in the high-order forest region and the N V $\lambda\lambda 1238, 1242$ doublet blended in the Ly α forest region, the C IV systems shown in the right panel are not necessarily include all the systems containing O VI and/or N V. Despite this incompleteness problem in detecting O VI and N V, most C VI systems with O VI and/or N V follow a similar trend displayed for Si IV-enriched and Si IV-free systems. This suggests that O VI and N V sample C IV systems over a wide range of physical conditions.

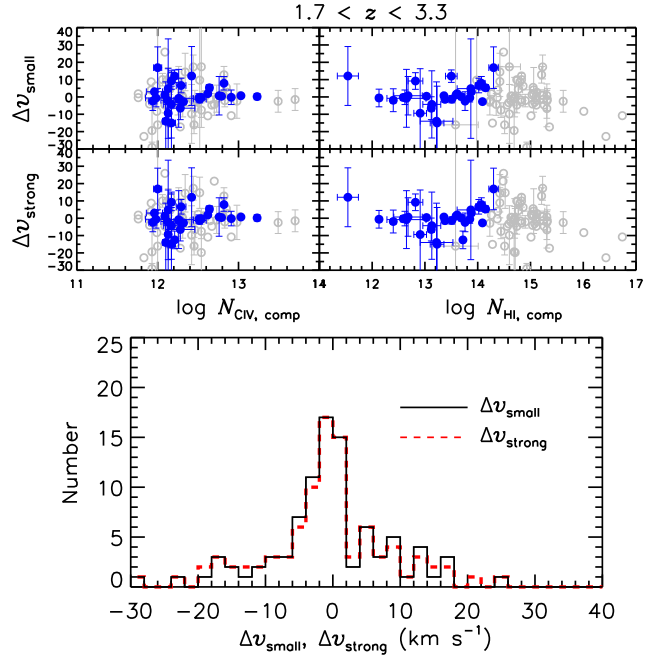


Figure 17. Upper panels: The velocity difference Δv_{small} in km s^{-1} between the C IV flux minimum and the closest H I component of 95 single-component C IV clumps as a function of $N_{\text{C IV, comp}}$ (left panel) and $N_{\text{H I, comp}}$ (right panel), respectively. Middle panels: The velocity difference Δv_{strong} between the C IV flux minimum and the strongest H I component of 95 single-component C IV clumps. Filled and open circles represent C IV components associated with unsaturated (Sample I) and saturated H I Ly α components (Sample II), respectively. Only errors larger than the symbol size are plotted. Lower panels: The number of all the aligned pairs as a function of Δv_{small} (the solid histogram) and of Δv_{strong} (the red dashed histogram).

7.2 [C/H] as an origin of the steep part of the integrated $N_{\text{H I}}-N_{\text{C IV}}$ relation

If we assume that [C/H], n_{H} and the UV background in a single C IV system does not vary significantly, the middle panel of Fig. 14 seems to suggest that the steep part of the integrated $N_{\text{H I}}-N_{\text{C IV}}$ relation could be caused by the right combination of [C/H] and n_{H} . There is no solid observational evidence on a constant [C/H], n_{H} and the UV background within a C IV system. However, as the steep $N_{\text{H I, sys}}-N_{\text{C IV, sys}}$ relation holds primarily for the Si IV-free and single-C IV-component C IV systems, they can be thought to sample a low-density region where the gas is optically thin and no radiative transfer effects complicate the internal structure of the absorption gas (Schaye et al. 2000; Schaye 2001; Shen et al. 2013).

Figure 19 presents the steep $N_{\text{H I, sys}}-N_{\text{C IV, sys}}$ relation overlaid with the CLOUDY predictions, when the fiducial Schaye $n_{\text{H}}-N_{\text{H I, comp}}$ relation was assumed. The data are well reproduced by absorbers with $[\text{C}/\text{H}] \in [-3.0, -1.5]$ and $\log n_{\text{H}} \in [-4.3, -3.5]$. Note that the CLOUDY-prediction for $[\text{C}/\text{H}] = -3.0$ even reproduces the sharp lower edge shown at $\log N_{\text{H I}} \in [15.0, 16.0]$.

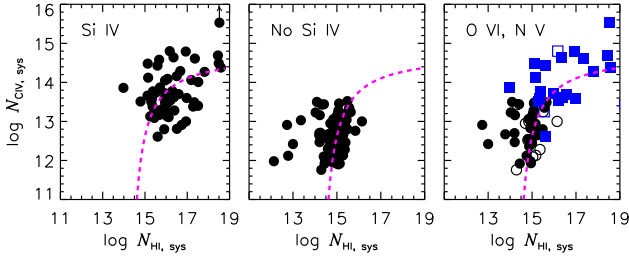


Figure 18. The integrated $N_{\text{HI}}-N_{\text{CIV}}$ relation of C IV systems associated with Si IV (left panel) and no Si IV (middle panel). Systems with blended, uncertain or unobserved Si IV regions are not included in the figures. In the right panel, circles and squares represent systems without and with associated Si IV, respectively. Filled and open symbols represent secure and uncertain detections of O VI and N V, respectively. The magenta dashed curve is the rectangular hyperbola fit as in Fig. 7.

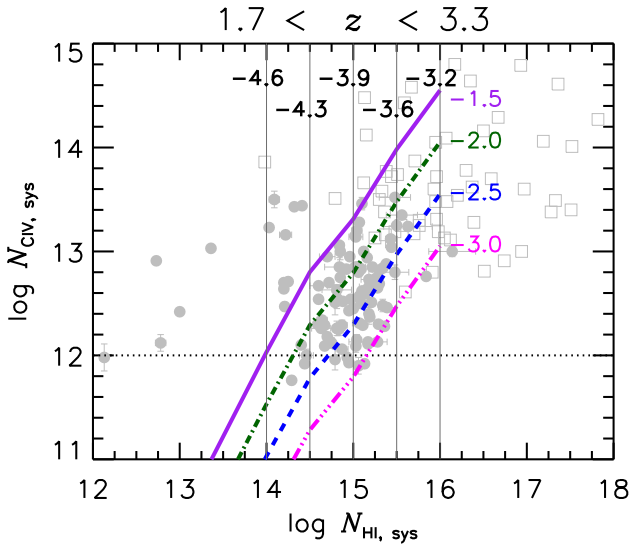


Figure 19. The integrated $N_{\text{HI}}-N_{\text{CIV}}$ relation of C IV systems overlaid with the CLOUDY predictions for a fixed $[\text{C}/\text{H}]$ noted next to each curve for the fiducial Schaye $n_{\text{H}}-N_{\text{HI, comp}}$ relation as a gray vertical line with its logarithmic n_{H} value on top. The C IV systems associated with Si IV and without Si IV are presented as open squares and filled circles. Systems with blended, uncertain or unobserved Si IV regions are not included. The dotted horizontal line presents the C IV detection limit.

7.3 Origins: Filaments and galactic halos

If the steep $N_{\text{HI, sys}}-N_{\text{CIV, sys}}$ relation for Si IV-free C IV systems is produced by the absorbing gas with $[\text{C}/\text{H}] \in [-3.0, -1.5]$ and $n_{\text{H}} \in [-4.3, -3.5]$, the two best candidates for the location of the gas are the IGM filaments close to the star-forming galaxies or the outer regions of intervening halos, cf. Fig. 1. Unfortunately, calculating a column density profile of H I and C IV as a function of impact parameter is not trivial. Even if the baryon density profile is assumed to follow the halo dark matter profile, conversion from the total hydrogen to H I requires an ionisation correction due to the UV background radiation and an interaction between out-

flows and inflows (Klar & Mücke 2008; Duffy et al. 2012; Thom et al. 2012).

For simplicity, we took a Navarro et al. (1997) (NFW) spherical dark matter density profile as the model for the H I density profile, $n_{\text{HI, NFW}}(r) = \frac{A}{r/x(1+r/x)^2}$, where r is a radial distance and the values of A and x vary from halo to halo. We note that the NFW profile successfully describes objects on large scales such as clusters and filaments, while it has difficulties on galaxy scales (Moore et al. 1999; Primack 2009; Governato et al. 2012). We also used a power-law gas density profile with $n_{\text{HI, iso}}(r) = B/r^2$ for an isothermal sphere.

The radial H I column density profile is then obtained by integrating $n_{\text{HI}}(r)$ along a line of sight through a halo at a given impact parameter ρ . For our NFW model,

$$N_{\text{HI, NFW}}(\rho) = 2 \int_{\rho}^R \frac{n_{\text{HI, NFW}}(r) r}{\sqrt{r^2 - \rho^2}} dr, \quad (3)$$

where R is a radius of a spherical halo in kpc, for ρ and r in kpc, $n_{\text{HI, NFW}}$ in cm^{-3} and $N_{\text{HI, NFW}}(\rho)$ in cm^{-2} .

For an isothermal sphere,

$$N_{\text{HI, iso}}(\rho) = B \left[\frac{\pi}{2\rho} - \frac{\arcsin(\rho/R)}{\rho} \right]. \quad (4)$$

Figure 20 shows these assumed $N_{\text{HI, sys}}$ profiles, including the simulated $N_{\text{HI, sys}}$ profile by Rauch et al. (1997) for an IGM filament centred at a protogalactic clump with the halo mass of $1.2 \times 10^9 M_{\odot}$. For the NFW model, we assumed a halo size of 100 kpc and took a value of $x = 16.1$ kpc as for the Milky Way (Nesti & Salucci 2013). Then, we varied the value of A roughly to match $\log N_{\text{HI, NFW}} \sim 14$ at 100 kpc based on Fig. 7. This leads to a dimensionless constant A of $\log A = 15.0$. We used a similar procedure to make an isothermal model to have $\log N_{\text{HI, iso}} \sim 14$ at 100 kpc.

Figure 20 also illustrates an expected $N_{\text{CIV, sys}}$ profile to reproduce the observed $N_{\text{HI, sys}}-N_{\text{CIV, sys}}$ relation for a given $N_{\text{HI, sys}}$ profile. The Rauch $N_{\text{CIV, sys}}$ profile gives an overall similar shape as our $N_{\text{HI, sys}}-N_{\text{CIV, sys}}$ relation, but follows the upper envelope of our data, implying that their simulation systematically overproduces $N_{\text{CIV, sys}}$ for a given $N_{\text{HI, sys}}$. When the ratio of $N_{\text{HI, sys}}$ and $N_{\text{CIV, sys}}$ is constant, a linear $N_{\text{HI, sys}}-N_{\text{CIV, sys}}$ relation is expected (the thin solid line in the right panel).

We note that our derived $N_{\text{CIV, sys}}$ profile depends on the assumed $N_{\text{HI, sys}}$ profile which is not likely to be correct and that our observed $N_{\text{HI, sys}}-N_{\text{CIV, sys}}$ relation is from an ensemble of many gas clouds along the line of sight passing galaxies and IGM filaments of different masses and sizes (see Fig. 1). As a more massive galaxy tends to have a larger halo and a higher star-formation rate (Brooks et al. 2011), our toy model of a 100 kpc halo size is too simplistic. Fortunately, the observed $N_{\text{HI, sys}}-N_{\text{CIV, sys}}$ relation is not a function of impact parameter, i.e. both integrated column densities are measured at the *same* impact parameter. Moreover, simulations have found that density profiles of halos and the surrounding IGM filaments are self-similar when scaled with the virial radius which is dependent on the galaxy mass (Pallottini et al. 2014). Therefore, our assumed column density profiles can be extended by multiplying the impact parameter axis by any number and the comparison of $N_{\text{HI, sys}}$ and $N_{\text{CIV, sys}}$ profiles at the same impact parameter does not depend on any assumed halo size.

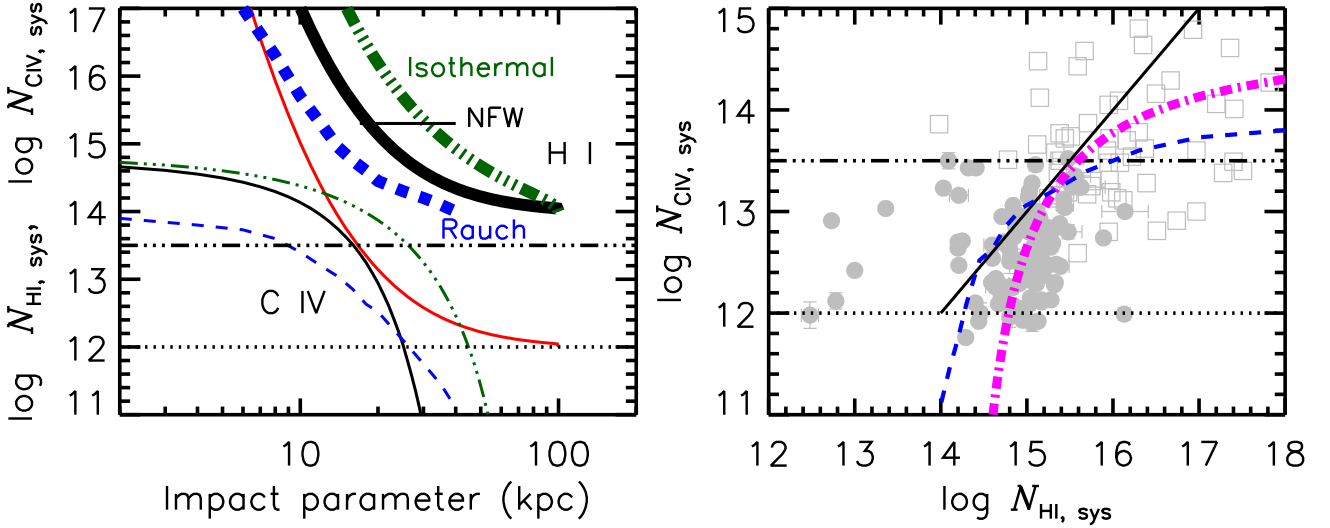


Figure 20. The left panel shows various profiles of $N_{\text{HI,sys}}$ (thick curves) and $N_{\text{CIV,sys}}$ (thin curves) as a function of impact parameter ρ in kpc. The thick solid and dot-dot-dot-dashed curves are an assumed $N_{\text{HI,sys}}$ profile for the NFW and isothermal density profiles, respectively, with the parameters matching $\log N_{\text{HI,sys}} \sim 14$ at 100 kpc, a size of an assumed intervening halo. The thin solid red curve is a $N_{\text{CIV,sys}}$ profile with $N_{\text{CIV,sys}}/N_{\text{HI,sys}} = 0.01$ for the shown $N_{\text{HI,NFW}}$ profile. Thick and thin blue dashed curves are $N_{\text{HI,sys}}$ and $N_{\text{CIV,sys}}$ profiles taken from Fig. 8 by Rauch et al. (1997) for a filament centred at a simulated protogalactic clump of $1.2 \times 10^9 M_{\odot}$. Their values are shown only upto 40 kpc. The black solid and dark green dot-dot-dot-dashed thin curves are the expected $N_{\text{CIV,sys}}$ profile to match the observed $N_{\text{HI,sys}}-N_{\text{CIV,sys}}$ relation (magenta dot-dashed curve) in the right panel for the NFW and isothermal models, respectively. The data points in the right panel are the same as in Fig. 19. In both panels, the horizontal dotted line represents our C IV detection limit, while the horizontal dot-dot-dashed line is the C IV detection limit of $\log N_{\text{CIV,gg}} = 13.5$ from the galaxy-galaxy pair study at $z \sim 2.2$ by Steidel et al. (2010).

Figure 20 implies that the $N_{\text{CIV,sys}}$ profile should be different from $N_{\text{HI,sys}}$ to reproduce the observed $N_{\text{HI,sys}}-N_{\text{CIV,sys}}$ relation, regardless of the assumed $N_{\text{HI,sys}}$ profile. $N_{\text{CIV,sys}}$ should have a rapid decrease compared to $N_{\text{HI,sys}}$ at closer to the halo size or the IGM filament size. As a result, the extent of C IV should be much smaller than H I above our detection limit of H I and C IV.

A similar trend has been found at $z \sim 2.2$ from the galaxy-galaxy pair study by Steidel et al. (2010). Their composite background galaxy spectrum shows a sharp decrease in the C IV rest-frame equivalent width (REW) at $\sim 80-90$ kpc above the C IV detection limit, the C IV REW of $\geq 0.15 \text{ \AA}$ (roughly $\log N_{\text{CIV}} \geq 13.5$). On the other hand, H I extends to a larger distance to ~ 250 kpc, but shows a similar rapid falloff in the H I REW at $\geq 0.31 \text{ \AA}$ (roughly $\log N_{\text{HI}} \geq 13.25$) around 250 kpc. The rapid falloff in $N_{\text{CIV,sys}}$ seems to continue to our smaller $N_{\text{CIV,sys}}$ range, implying that a line-of-sight C IV extent is not very different between $\log N_{\text{CIV,limit}} = 13.5$ and $\log N_{\text{CIV,limit}} = 12.0$.

We note that the $N_{\text{CIV,sys}}$ profiles displayed in Fig. 20 are different from those observed by Steidel et al. (2010). Their composite spectrum shows C IV absorption down to $\log N_{\text{CIV}} \sim 13.5$ at ~ 90 kpc, while the same $N_{\text{CIV,sys}}$ is expected at $\rho \sim 14$ kpc for our toy-model NFW profile. This discrepancy is mainly due to the direct comparison of column density profiles as a function of impact parameter without normalised by the virial radius. The Steidel sample mainly consists of galaxies bright enough to obtain a spectrum at $z \sim 2.2$, thus a higher column density at the same impact parameter than our 100 kpc toy-model halo.

The existence of a well-characterised $N_{\text{HI,sys}}-N_{\text{CIV,sys}}$

relation implies 1) a line-of-sight extent of the C IV gas is smaller than H I, 2) $N_{\text{CIV,sys}}$ decreases more rapidly than $N_{\text{HI,sys}}$ at the larger impact parameter, 3) their ratio can be well-characterised by a simple parameter, such as a potential of intervening halos or the IGM filament and 4) the integrated H I column density can be used as a proxy of normalised impact parameter.

7.4 Implications of the lack of evolution for the steep $N_{\text{HI,sys}}-N_{\text{CIV,sys}}$ relation

If we assume that a metal-enriched gas expands according to the Hubble flow as soon as it is placed in the surrounding IGM filament, ignoring any interaction with the infalling IGM, and that the gas temperature and the UV background do not change significantly at $z \sim 2.5$, then N_{HI} at the redshift z_2 becomes at the redshift z_1

$$\begin{aligned} N_{\text{HI}}(z_1) &= N_{\text{HI}}(z_2) \frac{n_{z_1} L_{z_1}}{n_{z_2} L_{z_2}} \\ &= N_{\text{HI}}(z_2) \frac{n_0 (1+z_1)^3}{n_0 (1+z_2)^3} \frac{L_0 (1+z_1)^{-1}}{L_0 (1+z_2)^{-1}}, \quad (5) \end{aligned}$$

where n_0 is the local gas density and L_0 is the local line-of-sight size. $N_{\text{HI,sys}}$ ($N_{\text{CIV,sys}}$) of the gas with $\log N_{\text{HI,sys}} = 15.2$ ($\log N_{\text{CIV,sys}} = 13.6$) at $\langle z \rangle = 2.80$ evolves to the gas with $\log N_{\text{HI,sys}} = 15.04$ ($\log N_{\text{CIV,sys}} = 13.44$) by $\langle z \rangle = 2.18$. This small difference makes virtually no evolution in the $N_{\text{HI,sys}}-N_{\text{CIV,sys}}$ relation, given a large spread in $N_{\text{CIV,sys}}$.

If the majority of Si IV-free C IV systems occur in the outskirts of an intervening halo due to outflows, the $N_{\text{HI,sys}}-N_{\text{CIV,sys}}$ relation at a given epoch should include a signature

of the outflows from previous starburst episodes happened before that epoch. Let us assume that the outflow velocity does not change. If the outflow launch velocity is assumed to be (100 km s^{-1} , 300 km s^{-1} , 600 km s^{-1}), the distance it travels during two epochs $z_2 = 2.80$ and $z_1 = 2.18$ is (72 kpc, 215 kpc, 430 kpc), respectively, for our assumed cosmology. Only outflows with a velocity $\geq 300 \text{ km s}^{-1}$ originating at $z > 2.8$ would have reached the virial radius of parent galaxies with $10^{11.7} M_\odot$ by $z = 2.18$. They would have been mixed with the surrounding IGM at $z < 2.18$ (Aguirre et al. 2001b).

Since more previous star-formation events are accumulated at lower redshifts and since more time is spent for metals to spread in the lower- N_{HI} IGM, the $N_{\text{HI, sys}} - N_{\text{CIV, sys}}$ relation would have shown a larger scatter at lower N_{HI} at lower redshifts. The fact that no such scatter is observed implies that 1) the terminal outflow velocity in the halo might be much lower than the escape velocity in general, i.e. the majority of metals stay inside a virial radius (Oppenheimer & Davé 2008), 2) each intervening halo is not likely to have several previous star-formation episodes at $z \sim 2.5$, and/or 3) the majority of outflow activities happen at $z \gg 3$, when a galaxy mass is lower, thus the escape velocity is also lower. Without later outflows, the $N_{\text{HI, sys}} - N_{\text{CIV, sys}}$ relation at $z \sim 2.5$ is only an asymptotic behaviour of outflows at $z > 3$, implying that most metals escaped to the surrounding IGM might have already been diluted below the detection limit (Aguirre et al. 2001b).

If most of Si IV-free C IV systems are at around the virial radius (Aguirre et al. 2001b; Oppenheimer & Davé 2008; Cen & Chisari 2011; van de Voort et al. 2011; Shen et al. 2013), the C IV-bearing halo gas is expected to have a similar behaviour to the C IV-bearing IGM filament gas, having its physical volume density close to the cosmic mean density. Therefore, we do not expect any significant redshift evolution at $z \in [1.7, 3.3]$.

8 CONCLUSIONS

We have presented the relations between N_{HI} and N_{CIV} of the 183 intervening C IV absorbers at $1.7 < z < 3.3$, based on the 23 high-resolution ($\sim 6.7 \text{ km s}^{-1}$) spectra obtained with UVES at the VLT and HIRES at Keck, with the detection limit of N_{HI} and N_{CIV} of $\log N_{\text{HI}} \sim 12.5$ and $\log N_{\text{CIV}} \sim 12.0$. As C IV is usually associated with saturated H I, we used all the available high-order Lyman lines to obtain a reliable component structure and a robust N_{HI} from the Voigt profile fitting analysis.

We define three terms to describe our H I+C IV sample, systems, clumps and components.

Systems: C IV system refers to all the H I and C IV components within a fixed velocity range centred at the C IV flux minimum, with the default of $\pm 150 \text{ km s}^{-1}$. When a C IV absorption extends over this velocity range or when a separate C IV absorption near $\pm 150 \text{ km s}^{-1}$ is seen beyond it, the velocity interval is extended to include additional C IV in that direction by steps of 100 km s^{-1} . Column densities integrated over this velocity range are averaged quantities.

Clumps: When the absorption wings of visibly separable C IV profiles recover to a normalised flux of 1 and a closest C IV absorption wing is more than 5 km s^{-1} away, this

distinct absorption feature is termed as a *clump*. All the H I components within the clump velocity range are assigned to that clump. When no H I exists, the clump velocity range is extended to include nearby H I components, depending on the profile shape of H I and C IV. A clump can consist of a single component or multiple components.

Components: The H I and C IV component pairs are grouped *well-aligned* if their velocity centroid differs by $\leq 5 \text{ km s}^{-1}$ and both are relatively clean. If nearby H I components make the line parameter of the aligned H I less reliable or if a C IV is located in a low-S/N region, the pairs are labelled as *reasonably-aligned*. Photoionisation modelling can be applied for aligned component pairs since they can be thought to be co-spatial.

From our 183 intervening C IV systems, we find:

(i) For about $\sim 75\%$ of the C IV systems (137/183), the integrated H I and C IV column densities, $N_{\text{HI, sys}}$ and $N_{\text{CIV, sys}}$, show a steep increase in $N_{\text{CIV, sys}}$ with $N_{\text{HI, sys}}$ at $\log N_{\text{HI, sys}} \in [14, 16]$, then becomes independent of $N_{\text{HI, sys}}$ at $\log N_{\text{HI, sys}} \geq 16$, with a large scatter in $\Delta \log N_{\text{CIV, sys}} = 2.5$ dex for a given $N_{\text{HI, sys}}$.

(ii) This $N_{\text{HI, sys}} - N_{\text{CIV, sys}}$ relation is best approximated as a rectangular hyperbola function at $\log N_{\text{HI, sys}} \in [14, 22]$ and at $\log N_{\text{CIV, sys}} \geq 11.8$:

$$\log N_{\text{CIV}} = \left[\frac{(-1.90 \pm 0.55)}{\log N_{\text{HI}} + (-14.11 \pm 0.19)} \right] + (14.76 \pm 0.17).$$

(iii) The $N_{\text{HI, sys}} - N_{\text{CIV, sys}}$ relation does not depend on the velocity range integrated over if it is $\geq \pm 100 \text{ km s}^{-1}$.

(iv) Assuming that the physical conditions in the gas do not change much within $\pm 150 \text{ km s}^{-1}$, the steep $N_{\text{HI, sys}} - N_{\text{CIV, sys}}$ relation can be reproduced by a gas with $[\text{C}/\text{H}] \in [-3.0, -1.5]$ and the total hydrogen volume density $\log n_{\text{H}} \in [-4.3, -3.5]$ under the Haardt-Madau QSOs+galaxies 2005 UV background and our fiducial Schaye $n_{\text{H}} - N_{\text{HI}}$ relation. The low $[\text{C}/\text{H}]$ and n_{H} suggest that the gas satisfying the steep $N_{\text{HI, sys}} - N_{\text{CIV, sys}}$ relation is likely to arise from a halo of intervening galaxies or the surrounding IGM filaments.

(v) C IV systems following the steep part of the $N_{\text{HI, sys}} - N_{\text{CIV, sys}}$ relation at $\log N_{\text{HI, sys}} \in [14, 16]$ are Si IV-free, consisting of one or two C IV components. The flat part of the relation at $\log N_{\text{HI, sys}} \in [16, 22]$ is dominated by Si IV-enriched systems, implying that they are produced by the gas with a higher physical volume density and/or a higher metallicity, i.e. galactic discs or inner haloes.

(vi) The steep $N_{\text{HI, sys}} - N_{\text{CIV, sys}}$ relation also requires that a line-of-sight extent of the C IV gas is smaller than the H I gas and that $N_{\text{CIV, sys}}$ decreases more rapidly than $N_{\text{HI, sys}}$ at the larger impact parameter above the detection limits, regardless of the location of the H I+C IV gas, i.e. intervening halos or IGM filaments. In addition, $N_{\text{HI, sys}}$ can be used as a proxy of normalised impact parameter by the virial radius.

(vii) There is a group of C IV systems (about 16%, 30/183) which do not follow the steep $N_{\text{HI, sys}} - N_{\text{CIV, sys}}$ relation at $(\log N_{\text{HI, sys}}, \log N_{\text{CIV, sys}}) = (12.0-14.0, 11.8-13.6)$. They have a higher $N_{\text{CIV, sys}}$ compared to C IV systems having a similar $N_{\text{HI, sys}}$. This higher- $N_{\text{CIV, sys}}$ can be obtained only by the gas with $[\text{C}/\text{H}] \in [0.0, 2.0]$ and $\log n_{\text{H}} \in [-4.3, -3.5]$ for the fiducial Schaye $n_{\text{H}} - N_{\text{HI}}$ relation, if the gas is close to the photoionisation equilibrium, implying that they are closely connected to star formation activities.

(viii) While there is no significant redshift evolution shown by the C IV systems following the $N_{\text{HI, sys}}-N_{\text{CIV, sys}}$ relation, the higher- $N_{\text{CIV, sys}}$ system only shows up predominantly at lower redshifts.

(ix) If the $N_{\text{HI, sys}}-N_{\text{CIV, sys}}$ relation holds at $\log N_{\text{CIV, sys}} \leq 11.8$, we expect very few C IV-enriched H I absorbers at $\log N_{\text{HI, sys}} \leq 14.0$ (or $N_{\text{HI, comp}}$), except rare higher- $N_{\text{CIV, sys}}$ absorbers.

As for 227 C IV clumps and 77 aligned H I+C IV components, we find:

(i) At $2.45 < z < 3.30$, the majority of C IV clumps follow the $N_{\text{HI, sys}}-N_{\text{CIV, sys}}$ relation. However, at $1.70 < z < 2.45$, there is no well-defined $N_{\text{HI, cl}}-N_{\text{CIV, cl}}$ relation, as C IV clumps start to show much larger scatters on the $N_{\text{HI, cl}}-N_{\text{CIV, cl}}$ plane. For the full redshift range, there exists no recognisable $N_{\text{HI, cl}}-N_{\text{CIV, cl}}$ relation.

(ii) For 95 single-C IV component clumps, the median velocity difference between closest H I and C IV component centroids is -0.6 km s^{-1} , with a 1σ dispersion of 11.3 km s^{-1} . The median velocity difference between C IV and strongest H I component is -0.6 km s^{-1} , with a dispersion of 11.6 km s^{-1} . The velocity smearing decreases a weak C IV flux by a factor of about 2 in the stacking analysis, but does not change the inferred $[\text{C}/\text{H}]$ significantly, given a large scatter seen in observational data.

(iii) For aligned components, there is no recognisable $N_{\text{HI, comp}}-N_{\text{CIV, comp}}$ relation at both redshift ranges, with more spread in data points farther away from the steep part of the $N_{\text{HI, sys}}-N_{\text{CIV, sys}}$ relation at lower redshifts.

(iv) There is a strong suggestion that there might be two separable C IV component groups at $1.70 < z < 2.45$. One group follows the steep part of the $N_{\text{HI, sys}}-N_{\text{CIV, sys}}$ relation with $\log(N_{\text{CIV, comp}}/N_{\text{HI, comp}}) \sim -2.4$, arising from the gas with $[\text{C}/\text{H}] \sim -2.5$ and $\log n_{\text{HI}} \sim -4.3$. Another group has a wider range of $N_{\text{CIV, comp}}/N_{\text{HI, comp}}$ with $\log(N_{\text{CIV, comp}}/N_{\text{HI, comp}}) \in [-1, 0]$, requiring $[\text{C}/\text{H}] \geq 0.0$ for the fiducial Schaye $n_{\text{HI}}-N_{\text{HI}}$ relation, possibly a consequence of increased star formation rates at $z \sim 2.1$.

ACKNOWLEDGMENTS.

We are grateful to M. Rauch, M. Viel, M. Haehnelt, J. Bolton and B. Savage for the insightful discussions. TSK acknowledges funding support from the European Research Council Starting Grant ‘‘Cosmology with the IGM’’ through grant GA-257670. RFC is also supported by the same grant for his stay at Osservatorio Astronomico di Trieste to carry out part of this work. TSK is also grateful to a travel support by the FP7 ERC Advanced Grant Emergence-320596 to IoA, Cambridge, where part of this work was done.

REFERENCES

Aguirre A., Hernquist L., Katz N., Gardner J., Weinberg D. H., Gardner J., 2001a, *ApJ*, 560, 599
Aguirre A., Hernquist L., Schaye J., Weinberg D. H., Katz N., Gardner J., 2001b, *ApJ*, 561, 521
Barai P., Monaco P., Murante G., Ragagnin A., Viel M., 2015, *MNRAS*, 447, 266
Boksenberg A., Sargent W. L. W., 2015, *ApJS*, 218, 7

Bolton J. S., Haehnelt M. G., Viel M., Springel V., 2005, *MNRAS*, 357, 1178
Bordoloi R., Lilly S. J., Kacprzak G. G., Churchill C. W., 2014, *ApJ*, 784, 108
Bouché N., Hohensee W., Vargas R., Kacprzak G. G., Martin C. L., Cooke J., Churchill C. W., 2012, *MNRAS*, 426, 801
Brooks A. M., et al., 2011, *ApJ*, 728, 51
Carswell R. F., Webb J. K., 2014, VPFIT, Astrophysics Source Code Library, record ascl:1408.015,
Carswell R. F., Schaye J., Kim T.-S., 2002, *ApJ*, 578, 43
Cen R., Chisari N. E., 2011, *ApJ*, 731, 11
Cen R., Miralda-Escudé J., Ostriker J. P., Rauch M., 1994, *ApJ*, 437, L9
Cowie L. L., Songaila A., Kim T.-S., Hu E. M., 1995, *AJ*, 109, 1522
D’Odorico V., et al., 2006, *MNRAS*, 372, 1333
D’Odorico V., Calura F., Cristiani S., Viel M., 2010, *MNRAS*, 401, 2715
Davé R., Hellsten U., Hernquist L., Katz N., Weinberg D. H., 1998, *ApJ*, 509, 661
Davé R., Hernquist L., Katz N., Weinberg D. H., 1999, *ApJ*, 511, 521
Davé R., Oppenheimer B. D., Katz N., Kollmeier J. A., Weinberg D. H., 2010, *MNRAS*, 408, 2051
Dessauges-Zavadsky M., Péroux C., Kim T.-S., D’Odorico S., McMahon R. G., 2003, *MNRAS*, 345, 447
Duffy A. R., Kay S. T., Battye R. A., Booth C. M., Dalla Vecchia C., Schaye J., 2012, *MNRAS*, 420, 2799
Ellison S. L., Songaila A., Schaye J., Pettini M., 2000, *ApJ*, 120, 1175
Erb D. K., Shapley A. E., Pettini M., Steidel C. C., Reddy N. A., Adelberger K. L., 2006, *ApJ*, 644, 813
Erb D. K., Quider A. M., Henry A.-L., Martin C. L., 2012, *ApJ*, 759, 26
Faucher-Giguère C. A., Kereš D., 2011, *MNRAS*, 412, 118
Faucher-Giguère C., Lidz A., Hernquist L., Zaldarriaga M., 2008, *ApJ*, 688, 85
Ferland G. J., Porter R. L., van Hoof P. A. M., Williams R. J. R., Abel N. P., Lykins M. L., Show G., et al. 2013, *RMxAA*, 49, 137
Fox A. J., Petitjean P., Ledoux C., Srianand R., 2007a, *A&A*, 465, 171
Fox A. J., Ledoux C., Petitjean P., Srianand R., 2007b, *A&A*, 473, 791
Gnedin N., 1998, *MNRAS*, 294, 407
Gnedin N., Ostriker J. P., 1997, *ApJ*, 486, 581
Governato F., et al., 2012, *MNRAS*, 422, 1231
Haiman Z., Loeb A., 1997, *ApJ*, 483, 21
Hui L., Gnedin N. Y., 1997, *MNRAS*, 292, 27
Jarosik N., et al., 2011, *ApJS*, 192, 14
Jenkins E. B., Bowen D. V., Tripp T. M., Sembach K. R., 2005, *ApJ*, 623, 767
Kacprzak G. G., Churchill C. W., Barton E. J., Cooke J., 2011, *ApJ*, 733, 105
Kim T.-S., Viel M., Haehnelt M. G., Carswell R. F., Cristiani S., 2004, *MNRAS*, 347, 355
Kim T.-S., Bolton J. S., Viel M., Haehnelt M. G., Carswell R. F., 2007, *MNRAS*, 382, 1657
Kim T.-S., Partl A. J., Carswell R. F., Müller V., 2013, *A&A*, 731, 6
Kim T.-S., Carswell R. F., Ranquist D., 2016, *MNRAS*, 456, 4
Klar J. S., Mücke J. P., 2008, *A&A*, 486, 25
Lehner N., Prochaska J. X., Kobulnicky H. A., Cooksey K. L., Howk J. C., Williger G. M., Cales S. L., 2009, *ApJ*, 694, 734
Lehner N., et al., 2013, *ApJ*, 770, 138
Lehner N., O’Meara J. M., Fox A. J., Howk J. C., Prochaska J. X., Burns V., Armstrong A. A., 2014, *ApJ*, 788, 119

- Levshakov S. A., Agafonova I. I., D'Odorico S., Wolfe A. M., Dessauges-Zavadsky M., 2003, *ApJ*, 582, 596
- Lu L., Savage B. D., 1993, *ApJ*, 403, 127
- Martin C. L., 2005, *ApJ*, 621, 227
- Martin C. L., 2006, *ApJ*, 647, 222
- McDonald P., Seljak U., Burles S., Schlegel D. J., Weinberg D. H., Cen R., 2006, *ApJS*, 163, 80
- Moore B., Quinn T., Governato F., Stadel J., Lake G., 1999, *MNRAS*, 310, 1147
- Murray N., Quataert E., Thompson T. A., 2005, *ApJ*, 618, 569
- Navarro J. F., Frenk C. S., White S. D. M., 1997, *ApJ*, 490, 493
- Nesti F., Salucci P., 2013, *jcap*, 7, 16
- Oppenheimer B. D., Davé R., 2006, *MNRAS*, 373, 1265
- Oppenheimer B. D., Davé R., 2008, *MNRAS*, 373, 577
- Oppenheimer B. D., Davé R., Katz N., Kollmeier J. A., Weinberg D. H., 2012, *MNRAS*, 420, 829
- Ostriker J. P., Gnedin N., 1996, *ApJ*, 472, 63
- Palanque-Delabrouille N., et al., 2013, *A&A*, 559, 85
- Pallottini A., Gallerani S., Ferrara A., 2014, *MNRAS*, 444, 105
- Penprase B. E., Prochaska J. X., Sargent W. L. W., Toromartinez I., Beeler D. J., 2010, *ApJ*, 721, 1
- Péroux C., Dessauges-Zavadsky M., D'Odorico S., Kim T.-S., McMahon R. G., 2007, *MNRAS*, 382, 177
- Pettini M., Rix S. A., Steidel C. C., Adelberger K. L., Hunt M. P., Shapley A. E., 2002, *ApJ*, 569, 742
- Pieri M. M., Frank S., Weinberg D. H., Mathur S., York D. G., 2010, *ApJ*, 724, 69
- Primack J. R., 2009, *NJPh*, 11, 105029
- Prochaska J. X., et al., 2001, *ApJS*, 137, 21
- Prochaska J. X., Lilly S. J., Kacprzak G. G., Churchill C. W., 2003, *ApJ*, 784, 108
- Prochaska J. X., O'Meara J. M., Herbert-Fort S., Burles S., Prochter G. E., Bernstein R. A., 2006, *ApJL*, 648, 97
- Rauch M., et al., 1997, *ApJ*, 489, 7
- Rauch M., Sargent W. L. W., Barlow T. A., 2001, *ApJ*, 554, 823
- Rauch M., Becker G. D., Viel M., Sargent W. L. W., Smette A., Simcoe R. A., Barlow T. A., Haehnelt M. G., 2005, *ApJ*, 632, 58
- Reimers D., Baade R., Hagen H. J., Lopez S., 2001, *A&A*, 374, 871
- Ribaud J., Lehner L., Howk J. C., 2011, *ApJ*, 736, 42
- Savage B. D., Sembach K. R., 1991, *ApJ*, 379, 245
- Savaglio S., et al., 1999, *ApJL*, 515, L5
- Schaye J., 2001, *ApJ*, 559, 507
- Schaye J., Theuns T., Rauch M., Efstathiou G., Sargent W. L. W., 2000, *MNRAS*, 318, 817
- Schaye J., Aguirre A., Kim T.-S., Theuns T., Rauch M., Sargent W. L. W., 2003, *ApJ*, 596, 768
- Schaye J., Carswell R. F., Kim T.-S., 2007, *MNRAS*, 379, 1169
- Sembach K. R., Savage B. D., 1992, *ApJS*, 83, 147
- Sembach K. R., Savage B. D., Massa D., 1991, *ApJ*, 372, 81
- Shapley A. E., Steidel C. C., Pettini M., Adelberger K. L., 2003, *ApJ*, 588, 65
- Shen S., Madau P., Guedes J., Mayer L., Prochaska J. X., Wadsley J., 2013, *ApJ*, 765, 89
- Simcoe R. A., Sargent W. L. W., Rauch M., 2004, *ApJ*, 606, 92
- Songaila A., 1998, *AJ*, 115, 2184
- Springel V., Hernquist L., 2003, *MNRAS*, 339, 289
- Steidel C. C., 1990, *ApJS*, 74, 37
- Steidel C. C., Erb D. K., Shapley A. E., Pettini M., Reddy N., Bogosavljević M., Rudie G. C., Rakic O., 2010, *ApJ*, 717, 289
- Stoeck J. T., Keeney B. A., Danforth C. W., 2010, *PASA*, 27, 256
- Strickland D. K., Heckman T. M., Colbert E. J. M., Hoopes C. G., Weaver K. A., 2004, *ApJ*, 606, 829
- Thilker D. A., Braun R., Walterbos R. A. M., Corbelli E., Lockman F. J., Murphy E., Maddalena R., 2004, *ApJL*, 601, 39
- Thom C., et al., 2012, *ApJL*, 758, L41
- Tremonti C. A., Moustakas J., Diamond-Stanic A.-M., 2007, *ApJ*, 663, L77
- Tumlinson J., et al., 2011, *Science*, 334, 948
- Tytler D., Fan X.-M., Burles S., Cottrell L., David C., Kirkman D., Zuo L., 1995, *QSO Absorption Lines*, ed. G. Meylan (Garching: ESO), p. 289
- Werk J. K., Prochaska J. X., Thom C., Tumlinson J., Tripp T. M., O'Meara J. M., Peebles M. S., 2013, *ApJS*, 204, 17
- Werk J. K., et al., 2014, *ApJ*, 792, 8
- Wiersma R. P. C., Schaye J., Smith B. D., 2009, *MNRAS*, 393, 99
- van de Voort F., Schaye J., Booth C. M., Haas M. R., Dalla Vecchia C., 2011, *MNRAS*, 414, 2458